Numerical investigation of turbulent aided mixed convection of liquid metal flow through a concentric annulus

L. Marocco [a,b,*], A. Alberti di Valmontana [b], Th. Wetzel [a]

[a] Karlsruhe Institute of Technology (KIT), Institute for Nuclear and Energy Technologies, Hermann-von-Helmholtz-Platz 1, 76344 Eggenstein-Leopoldshafen, Germany
[b] Politecnico di Milano, Department of Energy, via Lambruschini 4, 20156 Milan, Italy

Turbulent aided mixed convection of a liquid metal with $Pr = 0.021$ in a concentric heated annulus is investigated by solving the Reynolds-Averaged-Navier-Stokes equations. This geometry approximates rod bundles heat exchangers at high pitch-to-diameter ratios. Two inner-to-outer radius ratios of 0.13 and 0.5 are considered and a constant uniform heat flux is applied only to the inner wall, only to the outer wall or to both walls. Constant thermo-physical properties are assumed and buoyancy is accounted for in the momentum equation using the Boussinesq assumption. Four different eddy-viscosity models are first assessed against the few available experimental data for a pipe flow. The turbulent heat fluxes are modeled with the Simple-Gradient-Diffusion-Hypothesis and the turbulent Prandtl number is locally evaluated either with a correlation or by solving one additional transport equation for the temperature variance and one for its dissipation rate. The first approach gives a better agreement with the experimen-tal data. It is found that, compared to medium-to-high Prandtl number fluids, the Reynolds number has a much greater influence on the onset and magnitude of heat transfer impairment. Its extent and degree are less than for ordinary fluids. It is shown that, contrarily to a pipe flow where liquid metals with $Pr \approx 0.025$ behave similar to air or water, in the concentric annulus big differences exist. The reason is the considerable contribution of molecular heat transfer in liquid metals that compensates the reduced turbulent mixing due to buoyancy.

Keywords: Liquid metals, Mixed convection, Concentric annulus, Turbulence models

1. Introduction

The demand of reliable and clean energy at low prices poses a great challenge to the world. The study of liquid metals is very important for this purpose since they are considered excellent coolant fluids for many advanced applications. Their very large molecular conductivity, resulting in $Pr \sim \mathcal{O}(10^{-2} \div 10^{-3})$, makes them able to exchange energy more efficiently and with smaller surfaces than conventional fluids. Therefore they are attractive when the size and weight of the heat exchange devices should be limited and when high thermal loads are present. The underlying physical mechanism of heat transfer to liquid metals significantly differs from that of gases or ordinary liquids. Indeed, the contribution of the molecular thermal conduction to the total heat transfer is much higher for liquid metals than for order one and higher Prandtl number fluids.

Article history:
Received 11 August 2016
Received in revised form 29 September 2016
Accepted 30 September 2016

* Corresponding author at: Politecnico di Milano, Department of Energy, via Lambruschini 4, 20156 Milan, Italy.

E-mail address: luca.marocco@polimi.it (L. Marocco).

Convective heat transfer can be classified depending on which mechanism generates the flow motion.

- *Forced convection* occurs when external forces induce the flow
- *Natural convection* occurs when the flow is induced by gravitational forces due to density non-uniformity caused by temperature variations
- *Mixed convection* occurs when the previous modes act together, not as a simple superposition of effects but in a complex modification of flow and turbulence field

Mixed convection is encountered in many engineering applications, among others heat exchangers, nuclear and solar reactors, chemical plants and cooling of electronic components.

Depending on flow direction and thermal boundary conditions it can be classified in *aided* or *opposed* mixed convection. The first occurs for a vertical upward heated or downward cooled flow, i.e. when the buoyancy forces act in the same direction of the flow. Contrarily, opposed mixed convection occurs for a vertical downward heated or upward cooled flow, i.e. when the buoyancy forces act in the opposite direction of the flow. In laminar flows only the

Published Journal Article available at: http://dx.doi.org/10.1016/j.ijheatmasstransfer.2016.09.107

Nomenclature

Roman letters

Bo	Buoyancy number, Eq. (1) (–)
C_D	Darcy–Weisbach friction factor (–)
C_f/C_{f0}	mixed-to-forced friction factor ratio (–)
d_h	hydraulic diameter (m)
f	re-distribution function (–)
g	acceleration of gravity (m/s^2)
Gr_q	Grashof number, Eq. (2) (–)
k	turbulent kinetic energy (m^2/s^3)
k_θ	variance of temp. fluctuations, Eq. (16) (K^2)
Nu	Nusselt number (–)
Nu/Nu_0	mixed-to-forced Nusselt number ratio (–)
P^*	non-dimensional pressure $\frac{P-g x_i \delta_{i1}}{\rho u_b^2}$ (–)
Pe	Péclet number $Pe = RePr$ (–)
Pr	Prandtl number (–)
Pr_t	turbulent Prandtl number $Pr_t = \frac{\nu_t}{\alpha_t}$ (–)
q^*	non-dimensional molecular or turb. heat flux, (see Section 6.2) (–)
q_w^*	surface averaged wall heat flux, Eq. (25) (W/m^2)
q_w	wall heat flux (W/m^2)
r	radial coordinate (m)
r^*	non-dimensional radial coordinate $r^* = \frac{r-r_i}{r_o-r_i}$ (–)
Re	Reynolds number $Re = u_b d_h/\nu$ (–)
r	pipe radius (m)
S_{ij}	strain rate tensor $S_{ij} = 0.5\left(\frac{\partial u_i}{\partial x_j} + \frac{\partial u_j}{\partial x_i}\right)$ (s^{-1})
T	temperature (K)
T_{b0}	inlet bulk temperature (–)
u_i	velocity component (m/s)
u_i^*	non-dimensional velocity component u_i/u_b (–)
u^*	non-dimensional streamwise velocity (–)
u_b	bulk velocity (m/s)
$\overline{u'v'}^*$	non-dimensional Reynolds stresses (–)
$\overline{v^2}$	wall normal turbulent stress (m^2/s^2)
$\overline{v'T'}^*$	non-dimensional wall normal turbulent heat flux (–)
x_i	dimensional coordinate (m)
x_i^*	non-dimensional coordinate x_i/d_h (–)
y_w	distance from the nearest wall (m)

Greek letters

α	molecular thermal diffusivity (m^2/s)
α_t	turbulent thermal diffusivity (m^2/s)
β	thermal expansion coefficient (K^{-1})
δ	inner-to-outer radius ratio (–)
δ_{ij}	Kronecker delta (–)
ε	dissipation rate of k (m^2/s^3)
ε_θ	dissipation rate of k_θ, Eq. (17) (K^2/s)
$\tilde{\varepsilon}$	modified diss. rate of k, (see Section 4) (m^2/s^3)
λ	molecular thermal conductivity (W/m K)
ν	kinematic viscosity (m^2/s)
ν_t	turbulent kinematic viscosity (m^2/s)
θ	non-dimensional temperature $\theta = \frac{T-T_{b0}}{q^* d_h/\lambda}$ (–)

Subscripts

i	inner
o	outer
wi	inner wall
wo	outer wall

modifications of the velocity field due to buoyancy affect the heat transfer. For aided mixed convection heat transfer is enhanced, while it is impaired for opposing mixed convection. In turbulent flows not only the distortion of the velocity field (direct effect) due to buoyancy influences the heat transfer but also the consequent modifications of the turbulence field (indirect effect). A qualitative picture for fluids with Pr of about unity and above, for which diffusion of heat by turbulence is of dominant importance, can be given by referring to the flow inside a pipe [1,2]. When buoyancy forces oppose the flow, the velocity close to the pipe wall is retarded but at the same time the production of turbulent kinetic energy is enhanced. The second effect of increased turbulent mixing prevails and heat transfer is enhanced. For buoyancy aided mixed convection the flow is accelerated close to the wall. The modifications of the turbulence field initially imply a decrease of turbulent diffusion resulting in a less effective heat transfer. It then recovers at sufficiently high wall heat fluxes when the turbulence production increases again.

For fluids with a Prandtl number much lower than unity, diffusion of heat by turbulence can be of secondary importance and so, even if buoyancy significantly modifies the turbulence field, its effect on heat transfer can be no longer dominant. As shown experimentally and numerically by Jackson et al. [3], for liquid sodium ($Pr \sim \mathcal{O}(10^{-3})$) enhancement of heat transfer occurs with upward flow due to the increased advection and impairment occurs with downward flow. In fact the reduced influence of turbulence on energy transport across the pipe is the reason for the behavior analogous to that of a laminar flow.

Anyway, according to the experimental work of Buhr et al. [4] and to the numerical one of Cotton et al. [5], liquid metals with a higher Prandtl number like mercury ($Pr \sim \mathcal{O}(10^{-2})$) behave similarly to moderate Prandtl number fluids, such as air or water: heat transfer is impaired with modest buoyancy influence but recovers as buoyancy forces are increased.

Based on semi-empirical considerations, Jackson et al. [1] proposed the buoyancy number, Bo, defined in Eq. (1) to correlate the experimental data of mixed-to-forced Nusselt number ratios in a pipe or channel. Subsequently it has been used by many authors [3,6–10] to define the regions of pure forced, mixed and natural convection for fluids with $Pr \geqslant 0.7$.

$$Bo = 8 \cdot 10^4 \frac{Gr_q}{Re^{3.425} Pr^{0.8}} \tag{1}$$

$$Gr_q = \frac{g\beta d_h^4 q_w}{\nu^2 \lambda} \tag{2}$$

In obtaining Eq. (1), the Dittus-Boelter equation for forced convective heat transfer has been used. The latter is valid for medium-to–high Prandtl number fluids. For low Prandtl number fluids other correlations [5] and approaches [11] should be used, which lead to Bo number expressions different from Eq. (1). Anyway, the latter will be used throughout the present work in order to make a comparison with the results available for ordinary fluids.

The vast majority of experimental and numerical investigation of turbulent mixed convection have been done for air or water flowing inside a uniformly heated pipe [2,3,5,6,10,12–14], as this geometry finds widespread use in practical applications. The only studies the authors are aware of on mixed convection in concentric annuli are the experimental one with water of Wu et al. [8] and the numerical one for CO_2 close to the pseudo-critical point of Forooghi et al. [15] and Bae et al. [16]. They consider a single radius ratio of $\delta = 0.5$ and a heat flux applied on the inner wall. This geometry is particularly interesting and important for the analysis of more complex geometries like rod bundles at high pitch-to-diameter ratios. For the latter the friction factor and Nusselt number values

in the inner zone of an annulus can be considered as upper limits, as thoroughly discussed by Rehme [17].

In order to extend the knowledge on this topic, within this study the turbulent aided mixed convection to a liquid metal within a concentric annulus is numerically investigated using turbulence models. The simulations are performed for a liquid metal having $Pr = 0.021$ encompassing then mercury, gallium-indium-tin and lead–bismuth eutectic. Only aided mixed convection is considered because the heat transfer deterioration eventually occurring in this case can have detrimental effects on the heat exchange devices. Its correct prediction is then particularly important in the design phase of engineering applications. Two radius ratios are considered, namely $\delta = 0.13$ and $\delta = 0.5$. A uniform heat flux is applied to the inner wall, to the outer wall or to both walls to investigate all three possible thermal boundary conditions. A Reynolds number of $Re = 120000$ is used for the simulations, resulting in a Péclet number of $Pe = 3000$. This value has been chosen in order to have a significant contribution of the turbulent heat fluxes to heat transfer so that the effects of the modification of the turbulence field due to buoyancy can be analyzed. The buoyancy number is varied by varying Gr_q. The results are analyzed in terms of the mixed-to-forced Nusselt number and friction factor coefficient ratio at different Bo numbers. Their trends for the different radius ratios and wall heat flux combinations are explained by analyzing the corresponding fields of velocity, temperature, turbulent stresses, heat fluxes and turbulent-to-molecular thermal diffusivity ratio. Where necessary, simulations at $Pr = 0.85$ are also performed in order to highlight the different heat transfer mechanism between liquid metals and ordinary fluids.

2. Methodology

In this section the main methodological approach to the simulations is described together with the critical aspects addressed in this work regarding heat transfer modeling in liquid metal flows.

From the work of Kim et al. [18] and Keshmiri [14] on the assessment of several eddy-viscosity turbulence models by comparison with DNS data for air, it emerges that best performances are obtained with low-Re turbulence models whose damping functions do not depend on the dimensionless wall distance. Accordingly, in this work the Reynolds stresses are modeled using the $k-\varepsilon$ models of Launder and Sharma [19] (LS) and Abe et al. [20] (AKN) and the $k-\varepsilon-\overline{v^2}-f$ model of Durbin [21] with the modifications of [22,23] (V2F). It has to be pointed out that, as also experimentally observed by Rehme [24], in the flow through annuli with small radius ratio ($\delta < 0.1$) the position of zero shear stress is not coincident with the position of maximum velocity. Because the Boussinesq hypothesis to evaluate the Reynolds stresses implies the coincidence of the two positions, turbulence models based on it should give inaccurate results. Anyway, the radius ratios investigated in this work are $\delta > 0.1$ allowing then to use the above listed turbulence models.

The turbulent heat fluxes are modeled with the Simple Gradient Diffusion Hypothesis (SGDH). Accordingly, they are proportional to the mean temperature gradient through the turbulent viscosity and turbulent Prandtl number. As thoroughly discussed by Grötzbach [25], these standard eddy conductivity models based on the concept of a turbulent Prandtl number can be acceptable for buoyant flows with a boundary layer character, like the vertical pipe and annulus of the present investigation. Other than for medium and high Prandtl number fluids the assumption of a constant and almost unitary turbulent Prandtl number does not apply to liquid metals [25,26]. Two different approaches are then used to evaluate Pr_t. The first is by using the correlation of Kays [27] to locally evaluate Pr_t. This correlation has already been proven to perform well in liquid metal flows [26,28] and can be used with all the above listed turbulence models. The second approach aims at increasing the physical modeling of the turbulent heat fluxes by solving two additional transport equations, namely one for the temperature variance and one for its dissipation rate, in order to determine the turbulent thermal diffusivity by taking into account the dissimilarities between the thermal and dynamical turbulence fields. This model has been proposed by Manservisi and Menghini [29] and has also proven to give satisfactory results in several applications of liquid metal flows [26,30]. The damping functions and coefficients in the two additional equations have been tuned with the $k-\varepsilon$ model of Abe et al. [20]. Therefore it is only used in conjunction with this last turbulence model and in what follows it is designated as AKN-MA. The assessment of the model for a forced convective flow in an annular geometry can be found in [31]. The results agree well with experimental data from [32] at a given Péclet number. For different Péclet numbers the Nusselt number values evaluated with the model have been compared against two literature correlations for an annulus. These last return quite different Nusselt numbers with increasing Péclet number. This fact reflects once again the difficulties in obtaining reliable measurement data for liquid metal flows, as discussed in [33–35]. The results obtained with the AKN-MA model and the other turbulence models fall in between those of the correlations, so that a conclusion on the best performing model cannot be drawn. For low Pe the agreement with the correlations is satisfactory and the results of the AKN-MA model collapse together with those of the other turbulence models.

More advanced approaches like full second order differential models or Algebraic Heat Flux Models (AHFM) should improve the modeling capabilities of strong buoyant flows, where anisotropic heat transfer and counter-gradient heat fluxes occur [25]. Nevertheless, the large number of closure constants necessary for the first prevent them to be universal. Moreover, they are also numerically quite unstable. Algebraic heat flux models are directly deduced from the differential transport equations for the heat fluxes, retaining more physics than the SGDH. Some formulations of them have been already validated for natural convection air flows and they are a promising approach also for buoyant liquid metal flows. Anyway for the latter more validation is necessarily needed. A perspective of state-of-the-art approaches to heat flux modeling in liquid metal flows and future perspectives for research improvement is given by Roelofs et al. [36].

3. Governing equations

We consider the upward flow in a vertical concentric annulus of an incompressible Newtonian fluid with constant thermophysical properties and no viscous dissipation, with the influence of buoyancy accounted for with the Boussinesq approximation and with an uniform applied wall heat flux. The streamwise periodic non-dimensional steady-state Reynolds-averaged continuity, momentum and energy equations read as follows:

$$\frac{\partial u_i^*}{\partial x_i^*} = 0 \tag{3}$$

$$\frac{\partial\left(u_i^* u_j^*\right)}{\partial x_j^*} = -\frac{\partial P^*}{\partial x_i^*} + \frac{1}{Re}\left(1+\frac{\nu_t}{\nu}\right)\frac{\partial^2 u_i^*}{\partial x_j^* \partial x_j^*} - \left(\theta\frac{Gr_q}{Re^2} - \frac{C_D}{2}\right)\delta_{i1} \tag{4}$$

$$\frac{\partial(u_i^*\theta)}{\partial x_i^*} = \frac{1}{RePr}\left[\left(1+\frac{\nu_t}{\nu}\frac{Pr}{Pr_t}\right)\frac{\partial^2\theta}{\partial x_i^* \partial x_i^*} - 4u_i^*\delta_{i1}\right] \tag{5}$$

In the above equations the last two terms on the right-hand-side of Eqs. (4) and (5) arise from considering a periodic flow in the streamwise direction, as explained in [37]. They are retained for the fully-developed flow simulations of Section 6.2, while they

are omitted for the simulations of Section 6.1 where a developing flow is considered. Note also that the buoyancy term, i.e. $\theta \frac{Gr_q}{Re^2}$, in Eq. (4) is only accounted for in the streamwise direction.

4. Turbulence modeling

4.1. Turbulent viscosity, v_t

The constitutive equation of the turbulent viscosity for the models of AKN and LS is:

$$v_t = C_\mu f_\mu \frac{k^2}{\tilde{\varepsilon}} \tag{6}$$
$$T = \frac{k}{\tilde{\varepsilon}}$$

In the above equation f_μ and C_μ are a damping function to account for the near-wall effects and a constant, respectively.

The transport equations for the turbulent kinetic energy and dissipation rate solved for the LS, AKN and V2F models read as follows:

$$\frac{\partial(u_i k)}{\partial x_i} = \left(\nu + \frac{v_t}{\sigma_k}\right)\frac{\partial^2 k}{\partial x_i \partial x_i} + P_k - (\tilde{\varepsilon} - D) \tag{7}$$
$$\frac{\partial(u_i \tilde{\varepsilon})}{\partial x_i} = \left(\nu + \frac{v_t}{\sigma_\varepsilon}\right)\frac{\partial^2 \tilde{\varepsilon}}{\partial x_i \partial x_i} + C_{\varepsilon 1} f_1 \frac{P_k}{T} - C_{\varepsilon 2} f_2 \frac{\tilde{\varepsilon}}{T} + E \tag{8}$$

In the equations above $\tilde{\varepsilon} = \varepsilon + D$ is the modified dissipation of k and D is a damping function. This latter differs from zero only for the LS model. Thus in the AKN and V2F model is $\tilde{\varepsilon} = \varepsilon$ and the modified dissipation rate coincides with the true one. The production of turbulent kinetic energy due to shear, P_k, is computed with the Boussinesq hypothesis for the Reynolds stresses and reads as follows:

$$P_k = 2 v_t S_{ij} S_{ij} \tag{9}$$

The term E appearing in Eq. (8) differs from zero only for the LS model and it arises because of the use of the modified dissipation rate $\tilde{\varepsilon}$. The term accounting for turbulent kinetic energy production due to buoyancy has been omitted in Eqs. (7) and (8). Indeed, it has been found to be negligible in previous studies with air [13,18,14] and consequently it is expected to be also negligible for liquid metals because of the reduced contribution of turbulence on heat transfer for these fluids. Nevertheless, simulations have also been performed accounting for it and the results confirm its negligible contribution compared to the production term due to shear.

The constitutive equation of the turbulent viscosity for the V2F model is:

$$v_t = \min\left(0.09\frac{k^2}{\tilde{\varepsilon}}, C_\mu \overline{v^2} T\right) \tag{10}$$
$$T = \max\left(\frac{k}{\tilde{\varepsilon}}, 6.0\sqrt{\nu/\tilde{\varepsilon}}\right)$$

Apart from k and $\tilde{\varepsilon}$, two additional equations are solved, namely for the wall-normal turbulent stress, $\overline{v^2}$, and for the re-distribution function, f.

$$\frac{\partial\left(u_i \overline{v^2}\right)}{\partial x_i} = \left(\nu + \frac{v_t}{\sigma_k}\right)\frac{\partial^2 \overline{v^2}}{\partial x_i \partial x_i} - 6\overline{v^2}\frac{\tilde{\varepsilon}}{k} + \min\left(kf, -\frac{\tilde{\varepsilon}}{k}\left[(C_1 - 6)\overline{v^2} - \frac{2}{3}k(C_1 - 1)\right] + C_2 P_k\right) \tag{11}$$

$$L^2 \frac{\partial^2 f}{\partial x_i \partial x_i} - f - \frac{\tilde{\varepsilon}}{k}\left[(C_1 - 6)\frac{\overline{v^2}}{k} - \frac{2}{3}(C_1 - 1)\right] + C_2 \frac{P_k}{k} = 0 \tag{12}$$

$$L = C_L \max\left[\frac{k^{3/2}}{\tilde{\varepsilon}}, C_\eta\left(\frac{\nu^3}{\tilde{\varepsilon}}\right)^{1/4}\right]$$
$$C_1 = 1.4, \quad C_2 = 0.3, \quad C_\eta = 70, \quad C_L = 0.23$$

The common constants and parameters appearing in Eqs. (7)–(12) are summarized in Table 1 and the damping functions in Table 2. The boundary conditions at the walls for $k, \tilde{\varepsilon}, \overline{v^2}$ and f are listed in Table 4.

4.2. Turbulent Prandtl number, Pr_t

Two approaches are used to compute the turbulent Prandtl number. The first one adopts a correlation proposed by Kays [27] covering all molecular Prandtl numbers:

$$Pr_t = 0.85 + \frac{0.7}{Pr\frac{v_t}{\nu}} \tag{13}$$

Table 1
Closure constants and parameters in Eqs. (6)–(12).

Model	σ_k	σ_ε	C_μ	$C_{\varepsilon 2}$	$C_{\varepsilon 1}$	D	E
LS	1.0	1.3	0.09	1.92	1.44	$2\nu\left(\frac{\partial\sqrt{k}}{\partial x_i}\right)^2$	$2\nu v_t\left(\frac{\partial S}{\partial x_i}\right)^2$
AKN	1.4	1.4	0.09	1.90	1.50	0	0
V2F	1.0	1.3	0.22	1.90	1.4	0	0

$S = \sqrt{2S_{ij}S_{ij}}; S_{ij} = \frac{1}{2}\left(\frac{\partial u_i}{\partial x_j} + \frac{\partial u_j}{\partial x_i}\right)$

Table 2
Wall damping functions in Eqs. (6) and (8).

Model	f_1	f_2	f_μ
LS	1.0	$1 - 0.3\exp[-\min(R_t^2, 50)]$	$\exp\left[\frac{-3.4}{(1+R_t/50)^2}\right]$
AKN	1.0	$\left\{1 - 0.3\exp\left(-\left(\frac{R_t}{6.5}\right)^2\right)\right\}\left[1 - \exp\left(-\frac{R_y}{3.1}\right)\right]^2$	$\left[1 + \frac{5}{R_t^{3/4}}\exp\left(-\left(\frac{R_t}{200}\right)^2\right)\right]\left(1 - \exp\left(-\frac{R_y}{14}\right)\right)^2$
V2F	$1 + 0.05\min\left(\left(k/\overline{v^2}\right)^{0.5}, 100\right)$	1.0	–

$R_t = \frac{k^2}{\nu\tilde{\varepsilon}}; R_y = \frac{y_w(\nu\tilde{\varepsilon})^{1/4}}{\nu}$

Eq. (13) only depends on local quantities through v_t and has already been proven to perform satisfactorily in liquid metal flows [26,28]. This model is used in conjunction with the other flow turbulence models of Section 4.1 with the following designations: AKN-KAYS, LS-KAYS and V2F-KAYS.

The second approach is based on the work of Manservisi and Menghini [29]. The turbulent thermal diffusivity, and consequently Pr_t, is calculated with Eq. (14).

$$\alpha_t = C_\theta k \tau_{l\theta} \tag{14}$$

The local thermal characteristic time of turbulence is defined as follows:

$$\tau_{l\theta} = \frac{k}{\tilde{\varepsilon}}\left(f_{1\theta} Pr_{t\infty} + f_{2\theta}\right) \tag{15}$$

It is evaluated from the k and ε fields calculated with the AKN model together with the k_θ and ε_θ values obtained from the solution of the corresponding additional transport equations, Eqs. (16) and (17). Within this article this model is designated as AKN-MA.

$$\frac{\partial(u_i k_\theta)}{\partial x_i} = \left(\alpha + \frac{\alpha_t}{\sigma_{k_\theta}}\right)\frac{\partial^2 k_\theta}{\partial x_i \partial x_i} + P_\theta - \varepsilon_\theta \tag{16}$$

$$\frac{\partial(u_i \varepsilon_\theta)}{\partial x_i} = \left(\alpha + \frac{\alpha_t}{\sigma_{\varepsilon_\theta}}\right)\frac{\partial^2 \varepsilon_\theta}{\partial x_i \partial x_i} + \frac{\varepsilon_\theta}{k_\theta}\left(C_{p1} P_\theta - C_{d1}\varepsilon_\theta\right) + \frac{\varepsilon_\theta}{k}\left(C_{p2} P_k - C_{d2}\tilde{\varepsilon}\right) \tag{17}$$

The production of k_θ in Eq. (16) is evaluated according to the SGDH as:

$$P_\theta = \alpha_t \left(\frac{\partial T}{\partial x_i}\right)^2 \tag{18}$$

The definitions for the different parameters and damping functions are listed below, where R_y and R_t are defined in Table 2:

$$f_{1\theta} = \left(1 - \exp\left(-0.0526\sqrt{Pr} R_y\right)\right)\left(1 - \exp(-0.0714 R_y\right) \tag{19}$$

$$f_{2\theta} = f_{2a\theta}\frac{2R}{R + C_\gamma} + f_{2b\theta}\sqrt{\frac{2R}{Pr}}\frac{1.3}{\sqrt{Pr} R_t^{3/4}} \tag{20}$$

$$f_{2a\theta} = f_{1\theta}\exp(-4 \times 10^{-6} R_t^2) \tag{21}$$

$$f_{2b\theta} = f_{1\theta}\exp(-2.5 \times 10^{-5} R_t^2) \tag{22}$$

$$R = \frac{\varepsilon}{\varepsilon_\theta}\frac{k_\theta}{k} \tag{23}$$

$$C_{d2} = \left(1.9\left(1 - 0.3\exp(-0.0237 R_t^2)\right) - 1\right) \times \left(1 - \exp(-0.1754 R_y)\right)^2 \tag{24}$$

Eq. (23) accounts for the local ratio between the thermal and the hydrodynamic time scale, which are known to be very different in liquid metal flows. The constants appearing in Eqs. (14)–(17) and (19)–(22) are summarized in Table 3. The wall boundary conditions for k_θ and ε_θ are listed in Table 4.

5. Problem description and numerical setup

All simulations are performed on a 2D domain with the open source code OpenFOAM. Steady-state flow is assumed and the predictor–corrector SIMPLE algorithm [38] is used for the pressure–velocity coupling. The diffusion terms are discretized with a central-difference scheme while a linear upwind scheme is used for the convective terms. No-slip boundary conditions are enforced at the walls. Depending on the case studied, either a constant heat flux is applied to both walls or separately to the inner or outer wall, being the other one adiabatic. A zero gradient condition is used for all variables at the domain outlet.

The simulations of Section 6.2 refer to a fully developed flow and temperature field. Thus, cyclic boundary conditions are applied at the inlet and outlet of the domain, i.e. the values of the variables computed on the outlet face are mapped onto the inlet face. In obtaining Eqs. (4) and (5) the pressure and temperature have been subdivided in a periodic, constant part and in a part that varies linearly with the axial coordinate, resulting then in additional terms in both equations, as explained in Section 3. The actual values of pressure and temperature can then be simply retrieved by adding to the calculated values the linear contribution at each axial position [37]. In Eq. (4) the streamwise pressure gradient (inside the term C_D) is computed to satisfy the imposed mass flowrate, according to the specified Reynolds number.

The cases presented in Section 6.1 refer to a developing flow and temperature field. The actual pressure and temperature are now considered in Eqs. (4) and (5) and the last term in both equations is omitted. According to the experimental setup of the validation case [4], the inlet values of all variables, except the temperature, are set equal to those resulting from a previous simulation of a fully-developed pipe flow at the same Reynolds number. The temperature is set equal to a constant value.

A converged solution is assumed when all the following conditions are satisfied: (a) constant average drag coefficient on the walls; (b) constant average convective heat transfer coefficient on the walls; (c) scaled residuals of all variables below 10^{-6}.

The Grid Convergence Index method [39] is used to quantify the numerical discretization errors. Accordingly, the solution is computed for three different grids with a refinement ratio of 2. Two characteristic variables, namely the mixed-to-forced Nusselt number and friction factor ratio, are selected as representative for the

Table 3
Constants for the heat turbulence model.

C_θ	$\sigma_{k\theta}$	$\sigma_{\varepsilon\theta}$	C_{p1}	C_{d1}	C_{p2}	$Pr_{t\infty}$	C_γ
0.1	1.4	1.4	0.925	1.0	0.9	0.9	0.3

Table 4
Boundary conditions at the walls for the turbulence models.

Model	k	$\tilde{\varepsilon}$	$\overline{v^2}$	f	k_θ	ε_θ
LS	0	0	–	–	–	–
AKN	0	$2\nu\frac{k}{y_w^2}$	–	–	–	–
V2F	0	$2\nu\frac{k}{y_w^2}$	0	0	–	–
AKN-MA	0	$2\nu\frac{k}{y_w^2}$	–	–	0	$2\alpha\frac{k_\theta}{y_w^2}$

Table 5
Discretization errors using the GCI method. The results refer to the simulation of Section 6.2.4 with $Bo = 0.018$; Nu/Nu_0 and C_f/C_{f0} evaluated at outer heated wall; Grid refinement ratio of 2.

	Nu/Nu_0	C_f/C_{f0}
N_y	200, 400, 800	
ϕ_3	0.801	1.051
ϕ_2	0.794	1.059
ϕ_1	0.792	1.061
p	1.88	1.99
ϕ_{ext}^{32}	0.790	1.0622
ϕ_{ext}^{21}	0.791	1.0624
e_{ext}^{32}	0.36%	0.25%
e_{ext}^{21}	0.08%	0.07%
GCI^{32}	0.45%	0.31%
GCI^{21}	0.09%	0.08%

problem under consideration. The results for an exemplary case of Section 6.2.3 at a buoyancy number corresponding to strong laminarization are summarized in Table 5. The quantity ϕ_i refers to the calculated variable value, while the index $i = 1, 2, 3$ refers to the fine, medium and coarse grid respectively. The apparent order of the discretization method is denoted by p. The quantities ϕ_{ext}^{21} and e_{ext}^{21} and ϕ_{ext}^{32} and e_{ext}^{32} indicate the extrapolated values of the calculated variable and the errors on the medium-fine grid and medium-coarse grid, respectively. Both Nu/Nu_0 and C_f/C_{f0} show monotonic convergence.

A grid independent solution with a good accuracy, denoted by the low GCI values, is already obtained with the medium grid. This is then used for all simulations of Section 6.2. The GCI analysis has shown that 400 cells in the wall normal direction are necessary in order to obtain a grid independent solution. At least two points are located within a non-dimensional wall distance, y^+, less than one, 10 points within $y^+ \leqslant 5$ and 40 points within $y^+ \leqslant 30$, as required by the low-Re turbulence models of Section 4 and in order to properly resolve the hydro-dynamical and thermal boundary layers. For the fully developed cases considered in Section 6.2 the variables do not vary along the axial coordinate and the problem is practically monodimensional. Thus, the solution does not depend on the number of control volumes in this direction. In this work 20 cells are chosen. A much higher number of axial elements, $N_x = 500$, is used for the cases of Section 6.1, because of the developing flow and temperature fields.

6. Results

6.1. Validation

The experimental studies on mixed convection to liquid metals are not as extensive as those for fluids with a higher Prandtl number, also due to the difficulties related to the experimental investigation of these fluids [33–35]. Most of the studies are mainly devoted to show the distortion of the velocity profile under the influence of combined forced and free convection [40,41]. To the authors' knowledge, other than for sodium, the most reliable Nusselt number experimental data for liquid metals are still those of Buhr et al. [4] of 1974 for mercury. These have also been used by Cotton et al. [5] to assess the applicability of the LS model, together with a global correlation for the turbulent Prandtl number correlation, to turbulent aided mixed convection in a pipe.

Even though the present authors analyzed the aided mixed convection to a liquid metal with $Pr = 0.025$ flowing in a vertical annulus [32], their results are taken at a distance of $16\,d_h$ from the inlet, thus being in the developing region. Because the study of this work is focused on the fully developed mixed convection, the performance of the LS-KAYS, AKN-KAYS, V2F-KAYS and AKN-MA models are assessed by comparison with the data of [4] for a pipe. These are taken at $87\,d_h$ from the pipe inlet. Anyway, in order to avoid any possible discrepancies between the numerical results and the experimental data due to the flow being eventually not completely developed at the experimental axial position, the simulations are performed for a developing flow. In order to avoid any effects of the applied numerical boundary conditions on the simulation results at the measurement section, a domain length of $100\,d_h$ is considered.

From Fig. 1 good agreement with the experimental values is obtained with all turbulence models except the AKN-MA. This last is able to partly reproduce the trend of the experimental data but it strongly underestimates the magnitude of the laminarization. Because it uses the AKN model to predict k and $\tilde{\varepsilon}$, the reason for the discrepancy should lie in the values of Pr_t and consequently in the prediction of the turbulent heat fluxes. Indeed, as shown

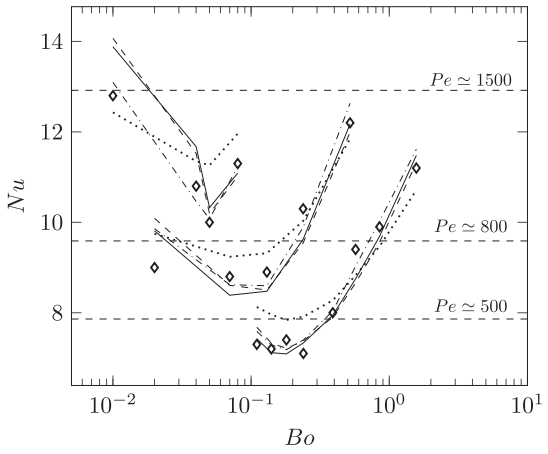

Fig. 1. Nusselt number comparison against experiments of Buhr et al. [4]. (——) LS-KAYS; (- - - -) AKN-KAYS; (-·-·-·-) V2F-KAYS; (·····) AKN-MA; (◇) Exp.; The dashed lines refer to forced convection Nusselt numbers computed with the correlation of Skupinski [33] for an average Péclet number from the experiments.

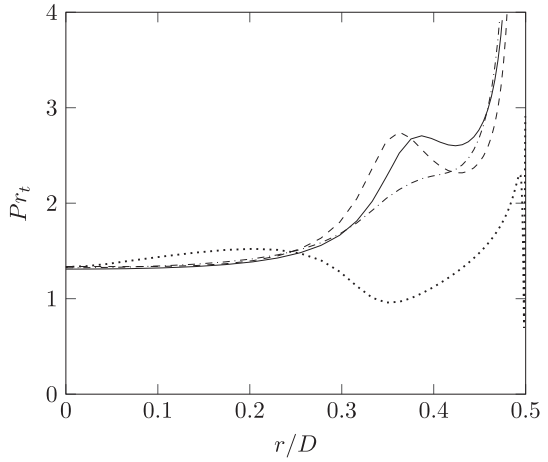

Fig. 2. Profiles of computed Pr_t for a pipe flow at $87\,d_h$, $Pe = 800$, $Pr = 0.025$ and $Bo = 0.13$. (——) LS-KAYS; (- - - -) AKN-KAYS; (-·-·-·-) V2F-KAYS; (·····) AKN-MA.

in Fig. 2, the AKN-MA model computes a much lower Pr_t resulting in a more effective turbulent heat transfer and consequently in higher Nusselt numbers.

According to the above results the AKN-MA will not be used for the subsequent simulations. Moreover, being the results of LS-KAYS, AKN-KAYS and V2F-KAYS almost coincident, only LS-KAYS is selected for the successive analysis. Indeed, the V2F is a four-equation model and thus computationally more expensive, while the non-zero wall boundary condition of ε makes the computations with the AKN model sometimes harder to converge. Furthermore, as already mentioned in Section 2, the LS model has already proven to perform well in several studies of aided mixed convection with fluids having $Pr \geqslant 0.7$.

From Fig. 1 it can also be noted how the magnitude, the onset and the extent of the heat transfer impairment strongly depends on the Péclet number. In order to study this effect, simulations with seven different Péclet numbers ranging from 500 to 3500 are carried out for the same $Pr = 0.021$. This results in a range of Reynolds numbers between 23800 and 166000. In Fig. 3 the calculated mixed-to-forced Nusselt number ratio is plotted against the buoyancy number. The results highlight that starting from $Pe = 2500$ the curves of Nu/Nu_0 practically overlap. Therefore, for

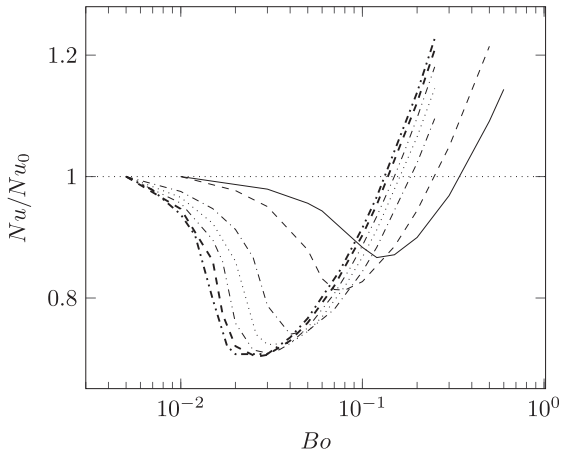

Fig. 3. Computed Nu/Nu_0 with LS-KAYS for a fully-developed pipe flow at $Pr = 0.021$. (——) $Pe = 500$; (- - - -) $Pe = 800$; (-·-·-·) $Pe = 1500$; (·····) $Pe = 2000$; (–··–··) $Pe = 2500$; (- - - -) $Pe = 3000$; (–·–·–·) $Pe = 3500$.

the analysis of the concentric annulus in Section 6.2 a Péclet number of $Pe = 3000$ has been chosen.

From Fig. 3 it can be immediately recognized that for decreasing Pe and thus Re numbers the onset of heat transfer impairment occurs at higher Bo numbers and its magnitude decreases. The reason lies in the higher molecular contribution to heat transfer at lower Reynolds numbers that compensates for the reduction of the turbulent heat fluxes. When moving to higher values of Pe the contribution of the turbulent thermal diffusion increases, even though it remains far below the levels reached in medium-to–high Prandtl number fluids. Therefore, due to a more prominent role of turbulence to heat transfer, its reduction is also felt earlier, i.e. at lower Bo numbers, and has a markedly higher impact on heat transfer implying lower values of Nu/Nu_0. According to Keshmiri [14] approximately the same behavior is found for a fluid with $Pr = 0.71$ but to a very much lesser extent than for liquid metals.

6.2. Concentric annulus

Other than for a circular pipe, where only one wall is present, in an annular pipe the same heat flux can be applied only to the inner, only to the outer or to both walls. In order to univocally define the buoyancy number for each thermal boundary condition, the wall heat flux in Eq. (2) is evaluated considering a surface weighted average from inner and outer wall, defined in Eq. (25).

$$q_w^* = q_{wi}\frac{\delta}{1+\delta} + q_{wo}\frac{1}{1+\delta} \tag{25}$$

Using Eq. (25) the same heat flux applied to the inner or to the outer wall results in two different Bo numbers in accordance to the different applied heat rate. In what follows, the streamwise velocity and Reynolds stresses are non-dimensionalized with u_b while the molecular and turbulent heat fluxes with $2q^*\alpha/\lambda$ resulting in $-\partial\theta/\partial r^*$ and $-\frac{\alpha_t}{\alpha}\partial\theta/\partial r^*$, respectively. Furthermore, the Nusselt number and friction factor results are normalized by the corresponding values evaluated for forced convection. As already explained by Kim et al. [18], this enables to better focus on the response of the models to mixed convection by limiting the effects due to different predictions of forced convection.

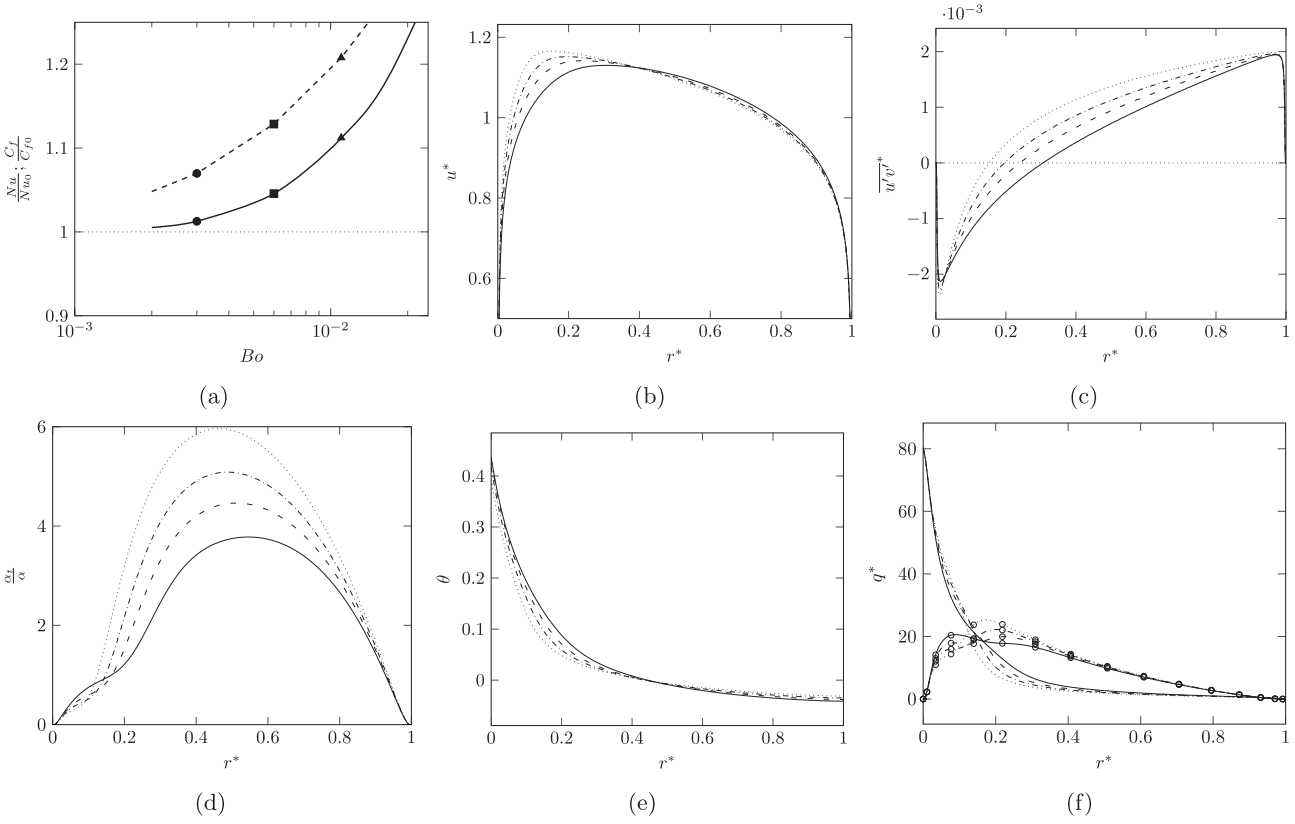

Fig. 4. Inner wall heated for $Pr = 0.021$ and $\delta = 0.13$ at (——) $Bo = 0$; (- - - -) $Bo = 0.003$; (-·-·-·) $Bo = 0.006$; (·····) $Bo = 0.011$ (a) Mixed-to-forced Nusselt number ratio (——) and skin friction ratio (- - - -); (b) Mean velocity profiles; (c) Reynolds stresses; (d) Turbulent-to-molecular diffusion; (e) non-dimensional temperature; (f) Molecular heat flux (lines without ○) and turbulent heat flux (lines with ○).

6.2.1. Inner wall heated and $\delta = 0.13$

Due to the small ratio between inner and outer wall areas, the region close to the outer wall is not affected by the inner wall heating and consequent modifications of the velocity and turbulence fields. Indeed for $r^* \geqslant 0.8$ the profiles for the different quantities shown in Fig. 4c–f tend to collapse together. With increasing *Bo* number the velocity peak moves towards the inner wall. Here the steeper velocity gradients prevail over the small reduction of turbulent mixing resulting in an increased mixed-to-forced ratio of skin friction coefficient, as shown in Fig. 4a. The velocity in the core region decreases in order to fulfill the requirement of constant mass flowrate. Anyway, this decrease is less pronounced than the corresponding velocity increase near the inner wall because of the growing flow areas at higher r^*. The peak of the Reynolds stresses is located almost at the same radial position and it increases a little with increasing *Bo*. Beyond the peak, the absolute value of $\overline{u'v'}^*$ first decreases and then grows fast when moving away from the inner wall and with increasing *Bo*. In these regions of high Reynolds stresses and comparable velocity gradients, the turbulent kinetic energy, and thus the turbulent momentum diffusivity, reaches higher values for the buoyancy affected flow cases compared to the forced convective one. This implies values of the turbulent-to-molecular thermal diffusivity ratio that grow above the corresponding forced convective ones and increase with increasing *Bo*. Only for $r^* \leqslant 0.17$ is the value of α_t/α lower than for forced convection. Anyway, as shown in Fig. 4f, this decrease is well balanced by the high molecular conduction of energy that is predominant in this zone. Therefore, the increased advective contribution to heat transfer due to the higher velocity values close to the inner wall and especially the higher values of α_t/α in the turbulent core result in an increased heat transfer. This is shown in Fig. 4a by the increase of the mixed-to-forced Nusselt number ratio as well as in Fig. 4e by the lower values of the non-dimensional wall temperature. It should also be noted that α_t is everywhere of the same order of magnitude of α, meaning that both the turbulent and the molecular heat flux contribute to the total heat flux all over the annular cross-section, as shown in Fig. 4f.

It is instructive to compare the results obtained for a liquid metal with $Pr = 0.021$ with those for an ordinary fluid with $Pr = 0.85$, the latter shown in Fig. 5. Even though the non-dimensional velocity and Reynolds stress profiles are similar to those of Fig. 4b and c for a liquid metal, it is immediately evident that the values of the turbulent thermal diffusivity are orders of magnitude higher than the corresponding molecular ones. Therefore, apart from the thin viscous thermal sublayer very close to the wall, the turbulent heat fluxes alone contribute to the total heat flux over practically the entire cross section, as shown in Fig. 5f. Therefore, at the three *Bo* numbers considered in Fig. 5, the decrease of the turbulent heat fluxes for $r^* \leqslant 0.1$, due to the decreased values of α_t/α, is not balanced by the increased advection due to the higher velocities (Fig. 5b). The heat transfer is thus reduced. The reduction is anyway very small because the decrease of α_t/α is only confined to a narrow region very close to the inner wall. The maximum impairment occurs at $Bo = 0.018$, corresponding to the lowest values of α_t/α and $\overline{v'T'}^*$ all over $0 \leqslant r^* \leqslant 0.1$. With increasing *Bo* the heat transfer recovers fast because the values of the turbulent thermal diffusivity tend to increase above those for forced convection at every r^*.

It should be noted the different heat transfer mechanism acting for very low Prandtl number fluids like liquid metals and ordinary fluids like air. Indeed, for the first the very high thermal conductivity and consequently molecular heat fluxes dampen the reduced

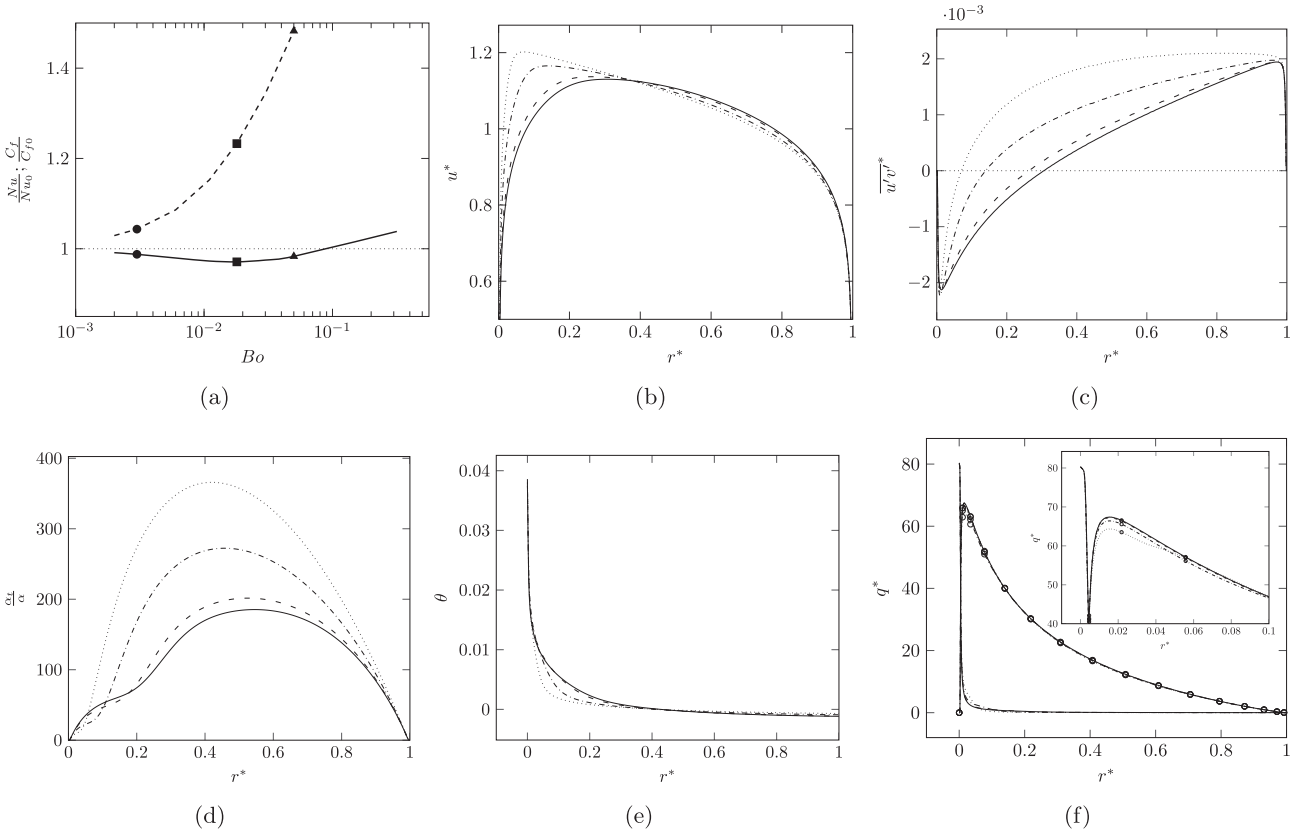

Fig. 5. Inner wall heated for $Pr = 0.85$ and $\delta = 0.13$ at (——) $Bo = 0$; (- - - -) $Bo = 0.003$; (-·-·-) $Bo = 0.018$; (·····) $Bo = 0.050$ (a) Mixed-to-forced Nusselt number ratio (——) and skin friction ratio (- - - -); (b) Mean velocity profiles; (c) Reynolds stresses; (d) Turbulent-to-molecular diffusion; (e) non-dimensional temperature; (f) Molecular heat flux (lines without ○) and turbulent heat flux (lines with ○).

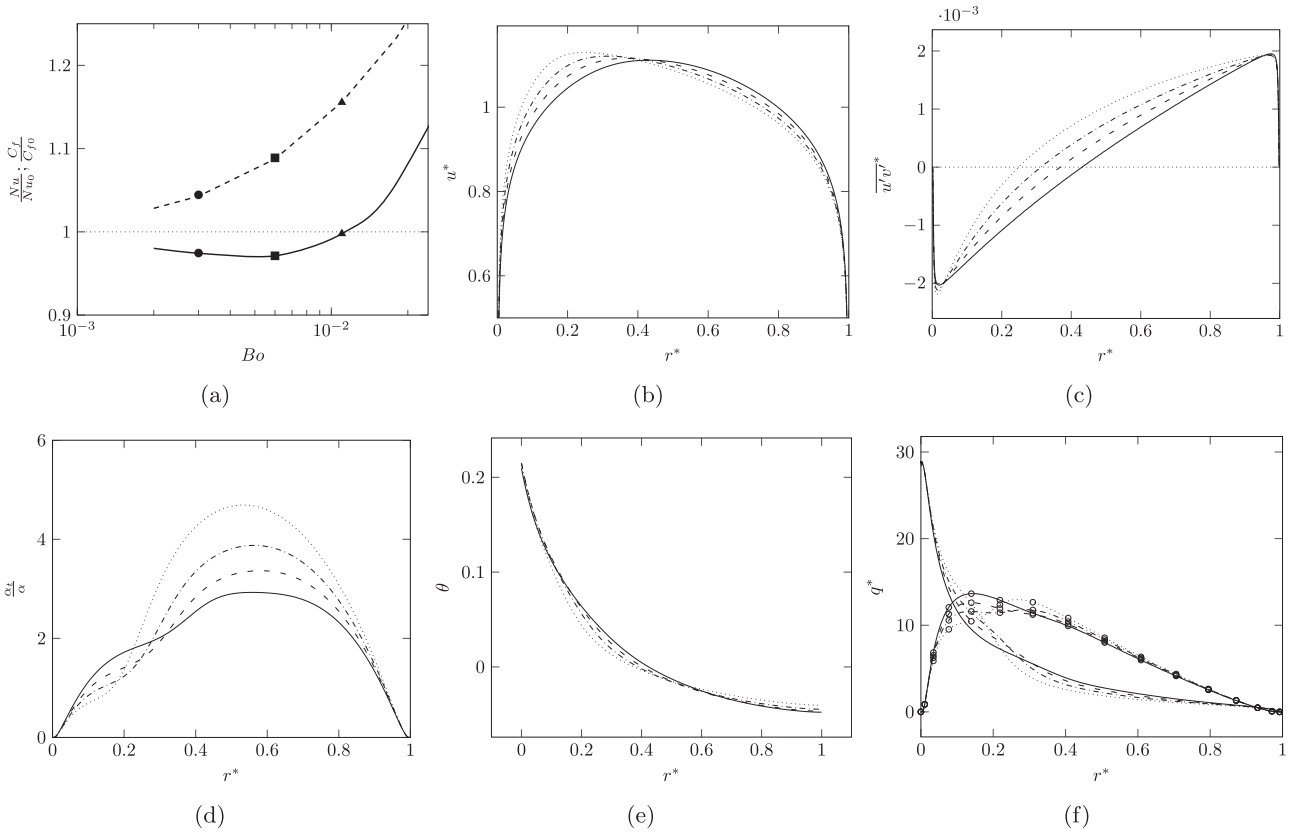

Fig. 6. Inner wall heated for $Pr = 0.021$ and $\delta = 0.5$ at (——) $Bo = 0$; (- - - -) $Bo = 0.003$; (- - - -) $Bo = 0.006$; (·····) $Bo = 0.011$ (a) Mixed-to-forced Nusselt number ratio (——) and skin friction ratio (- - - -); (b) Mean velocity profiles; (c) Reynolds stresses; (d) Turbulent-to-molecular diffusion; (e) non-dimensional temperature; (f) Molecular heat flux (lines without ○) and turbulent heat flux (lines with ○).

turbulent thermal diffusivity close to the wall. At this radius ratio the heat transfer is thus always enhanced. For air the turbulent heat fluxes dominate the heat transfer process and their reduction close to the inner heated wall causes then a decrease of heat transfer and thus Nusselt number.

6.2.2. Inner wall heated and $\delta = 0.5$

At the same *Bo* numbers or wall heat fluxes, the energy introduced into the system is now approximately four times higher than for $\delta = 0.13$. The peak of the non-dimensional velocity profiles still shifts towards the inner heated wall and the profiles become steeper in this region. As for the previous case with $\delta = 0.13$ the higher velocity gradients prevail over the small reduction of turbulent mixing resulting in a monotonically increasing mixed-to-forced ratio of skin friction coefficient, as shown in Fig. 6a. Contrarily, the Nusselt number ratio first decreases and then increases, confirming the less direct relationship between momentum and heat transfer in buoyancy influenced flows compared to forced convection ones. Because of the fixed mass flowrate the non-dimensional velocity in the core and in the outer wall region must decrease. Compared to the previous case with $\delta = 0.13$ a larger cross sectional area is now interested by the modified profiles. Moreover, the position of maximum velocity is now located closer to the pipe center. The velocity gradients and the Reynolds stresses are everywhere smaller compared to the case with $\delta = 0.13$ and so are the production of turbulent kinetic energy and the turbulent kinetic energy itself. As a consequence, also the values of α_t/α are lower. As can be appreciated from Fig. 6d the region where α_t/α is lower than for forced convection extends now to $r^* \leqslant 0.3$, where the turbulent heat fluxes are already much higher than the molecular ones, as shown in Fig. 6f. This, together with the overall reduced levels of turbulent thermal diffusivity compared to $\delta = 0.13$, causes a decrease in the Nusselt number for $Bo = 0.003$ and $Bo = 0.006$. At $Bo = 0.011$, even though approximately for $r^* \leqslant 0.2$ the values of α_t/α are still lower than those for forced convection, the Nusselt number has recovered reaching again the forced convection value. Indeed, for $r^* \leqslant 0.2$ the molecular heat fluxes are either equal or higher than the turbulent ones, while elsewhere the increased level of turbulent thermal diffusivity at this *Bo* number promotes the energy transfer process.

6.2.3. Outer wall heated and $\delta = 0.13$

This case is similar to a heated circular tube because of the small area of the inner wall. With increasing *Bo* number, the velocity peaks shift towards the outer heated wall, resulting in completely modified velocity profiles. The Reynolds stresses increase close to the inner wall, where also the velocity gradients become higher. They decrease close to the outer wall until reaching the position of peak velocity and then increase again but with opposite sign. The consequent decrease of momentum turbulent diffusivity close to the outer wall is balanced by the increased velocity gradients, resulting in a monotonically increase of the friction factor coefficient, as shown in Fig. 7a. From the same figure the dissimilarity between momentum and heat transfer is evident.

For $Bo = 0.018$ the values of $\overline{u'v'}^*$ remain lower than the corresponding ones for forced convection for $r^* \geqslant 0.4$. In the same interval are the values of α_t/α also lower than for $Bo = 0$. The turbulence decrease extends then well into the region where even for liquid metals the turbulent heat fluxes contribute more than the molecular ones to the energy transfer, as shown in Fig. 7f. For $Bo = 0.018$ $\overline{v'T'}^*$ show the lowest value over most of the cross

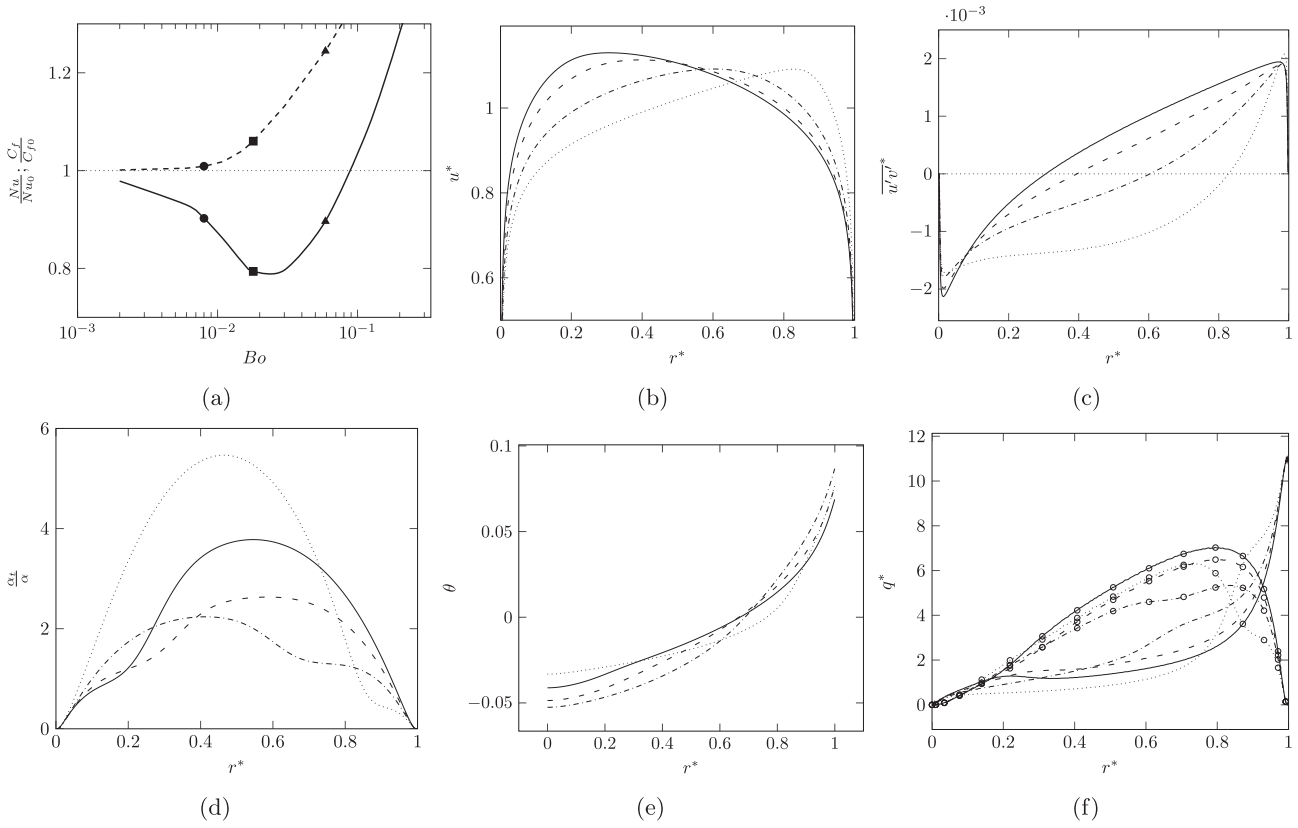

Fig. 7. Outer wall heated for $Pr = 0.021$ and $\delta = 0.13$ at (——) $Bo = 0$; (- - - -) $Bo = 0.008$; (-·-·-·) $Bo = 0.018$; (·····) $Bo = 0.059$ (a) Mixed-to-forced Nusselt number ratio (——) and skin friction ratio (- - - -); (b) Mean velocity profiles; (c) Reynolds stresses; (d) Turbulent-to-molecular diffusion; (e) non-dimensional temperature; (f) Molecular heat flux (lines without ○) and turbulent heat flux (lines with ○).

section. The Nusselt number attains therefore its lowest value and the temperature has the roundest profile (Fig. 7e).

At $Bo = 0.059$ the flow is in the recovery region, being the value of the Nusselt number almost the same as for $Bo = 0.008$. As shown in Fig. 7b the velocity profile is almost a mirror-image of the forced convective one. The remarkable increase of mass flowrate at high r^* due to the high velocity values must be balanced by a large velocity decrease at lower values of non-dimensional radius and thus cross sectional flow areas. The resulting steeper velocity profiles and the consequently larger velocity gradients promote the production of turbulent kinetic energy, which reflects in values of $\overline{u'v'}^*$ (magnitude) and α_t/α now even above the forced convective ones for approximately $r^* \leqslant 0.7$. In the vicinity of the outer wall, for $r^* \geqslant 0.8$, the values of α_t/α are lower than for $Bo = 0.008$ and $Bo = 0.018$. Nevertheless, as shown in Fig. 7f, the molecular heat fluxes compensate here for the reduced turbulent ones. Their high value is a consequence of the increased velocity and therefore of the advective contribution to heat transfer. From Fig. 7e it can be noted how, compared to the other Bo numbers, the temperature profile for $Bo = 0.059$ is steeper close to the heated wall, resulting in higher values of temperature gradients, and how it is flatter where α_t/α and thus the turbulent heat fluxes attain higher values.

The results for liquid metals can be qualitatively compared to those available in literature for medium-to–high Prandtl number fluids for aided mixed convection in a round pipe. For the latter, contrarily to low-Pr number fluids, the turbulent heat fluxes are orders of magnitude higher than the molecular ones over practically the entire cross section. Moreover, the thermal sublayer, where the molecular heat fluxes predominate, is confined to a very thin region in the immediate wall proximity. Contrarily to liquid metals, the recovery of heat transfer then occurs only when the values of α_t/α close to the heated wall at a specified Bo grow beyond those corresponding to maximum heat transfer impairment.

6.2.4. Outer wall heated and $\delta = 0.5$

Contrarily to the case with $\delta = 0.13$, the presence of the unheated inner wall has now a much more pronounced influence, as also shown by the more symmetric velocity profile of Fig. 8b. The rounder profiles of u^* for $Bo = 0$ and consequently the smaller velocity gradients result in a smaller turbulent production of kinetic energy. This implies overall lower values of α_t/α and $\overline{v'T'}^*$ compared to the corresponding case with $\delta = 0.13$. Moreover, due to the lower turbulence intensity, also the reduction of α_t/α with respect to $Bo = 0$ is smaller. The monotonic increase of friction factor shown in Fig. 8a is a consequence of the direct effect of buoyancy on the velocity field close to the outer wall. This results in higher velocity gradients, that prevail over the indirect effect caused by the reduction of turbulent momentum mixing.

Compared to the previous case with $\delta = 0.13$, the reduction of $\overline{u'v'}^*$ and α_t/α for $Bo = 0.008$ and $Bo = 0.018$ is limited to $r^* \geqslant 0.4$ and $r^* \geqslant 0.6$ respectively, thus to a smaller range of r^*. Together with the lower relative reduction of α_t/α, this implies a much smaller heat transfer impairment, as shown in Fig. 8 by the higher values of the Nusselt number ratio at $Bo = 0.018$. Moreover, because of the overall lower forced convection values of α_t/α, also the recovery occurs earlier. Indeed, the values of turbulent thermal diffusivity and thus of turbulent thermal heat fluxes grow beyond the corresponding ones for $Bo = 0$ already at lower Bo. Therefore,

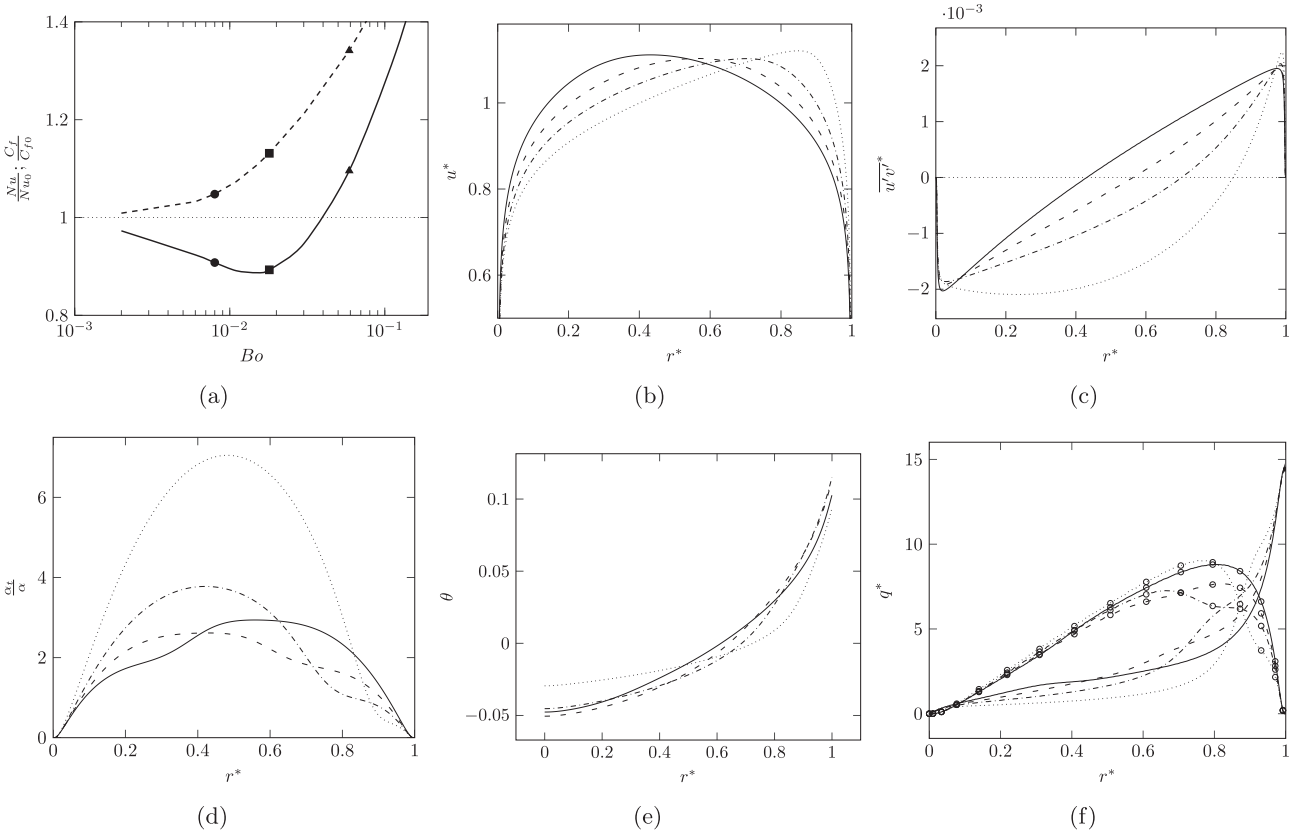

Fig. 8. Outer wall heated for $Pr = 0.021$ and $\delta = 0.5$ at (——) $Bo = 0$; (- - - -) $Bo = 0.008$; (-·-·-·-) $Bo = 0.018$; (·····) $Bo = 0.059$ (a) Mixed-to-forced Nusselt number ratio (——) and skin friction ratio (- - - -); (b) Mean velocity profiles; (c) Reynolds stresses; (d) Turbulent-to-molecular diffusion; (e) non-dimensional temperature; (f) Molecular heat flux (lines without ○) and turbulent heat flux (lines with ○).

the region of heat transfer impairment reduces strongly. At $Bo = 0.059$ the Nusselt number ratio is now higher than unity even though for $r^* \geqslant 0.9$ the values of α_t/α are lower than for the other two buoyancy numbers and for $Bo = 0$ and become higher than for forced convection only for $r^* \leqslant 0.8$. As already discussed before, the reason lies in the contribution of the molecular heat fluxes that compensate for the lower turbulent heat fluxes, as shown in Fig. 8f. Compared to the case with $\delta = 0.13$, the non-dimensional temperature profiles shown in Fig. 8e are now steeper close to the heated wall, where the Nusselt number ratio is higher, and flatten towards the inner unheated wall where the turbulent thermal diffusion is high.

6.2.5. Both walls heated and $\delta = 0.13$

As can be appreciated from Fig. 9b–d, the profiles of u^*, $\overline{u'v'}^*$, α_t/α and $\overline{v'T'}^*$ for the outer wall practically coincide with those of Fig. 7b–d when only the outer wall is heated. Indeed, the inner wall area and inner wall heat rate are only 13% of the outer wall ones.

As shown in Fig. 9a, the profile of C_f/C_{f0} on the inner wall first decreases at $Bo = 0.015$ and $Bo = 0.026$, when the velocity profile becomes flatter and the Reynolds stresses decrease below the forced convective values. It then recovers at higher Bo numbers when $\overline{u'v'}^*$ grow and thus the turbulent mixing recovers. At the outer wall the steep velocity gradients always cause an increase of C_f/C_{f0} for all Bo numbers.

The strong increase of the Nusselt number ratio on the inner wall for $Bo = 0.026$ cannot be explained with the same reasoning used in Section 6.2.1 for $\delta = 0.13$ and only the inner wall heated. Indeed, the profiles of u^*, $\overline{u'v'}^*$, α_t/α now completely differ from those shown in Fig. 4b–d. The velocity close to the inner wall, and thus the advective contribution to heat transfer, is now lower than for $Bo = 0$ and also α_t/α is lower for $r^* \geqslant 0.2$. The explanation for the Nusselt number increase can be given by considering the constraint of constant applied heat flux on the inner wall surface and the non-dimensional bulk temperature, that from its definition equals zero (note that when solving Eq. (5) for a periodic flow the dimensional bulk temperature is constant along the flow direction and equal to T_{b0}). This last condition is equivalent to:

$$\int_A u^* \theta dA = 0 \tag{26}$$

As shown in Fig. 9d and e, a heat transfer impairment on the outer surface implies an increase of the non-dimensional outer wall temperature and reduced turbulent thermal diffusivity over the radius. The temperature profiles are rounder than the corresponding one for $Bo = 0$ because of the reduced turbulent mixing. When approaching the inner wall, the constraint of constant applied (positive) heat flux must be fulfilled, together with Eq. (26). Therefore the non-dimensional temperature profile has an inflection and increases until reaching the (positive) temperature value at the wall. According to Eq. (26), the higher is the temperature value on the outer wall the lower is it on the inner wall. The resulting high temperature gradients imply high molecular heat fluxes (Fig. 9f) that contribute to the heat transfer enhancement and to higher Nusselt number values. At $Bo = 0.118$, during heat transfer recovery on the outer wall, θ_{wo} decreases and the turbulent contribution to heat transfer increases over the cross section (Fig. 9f), as also shown by the flattening of the temperature

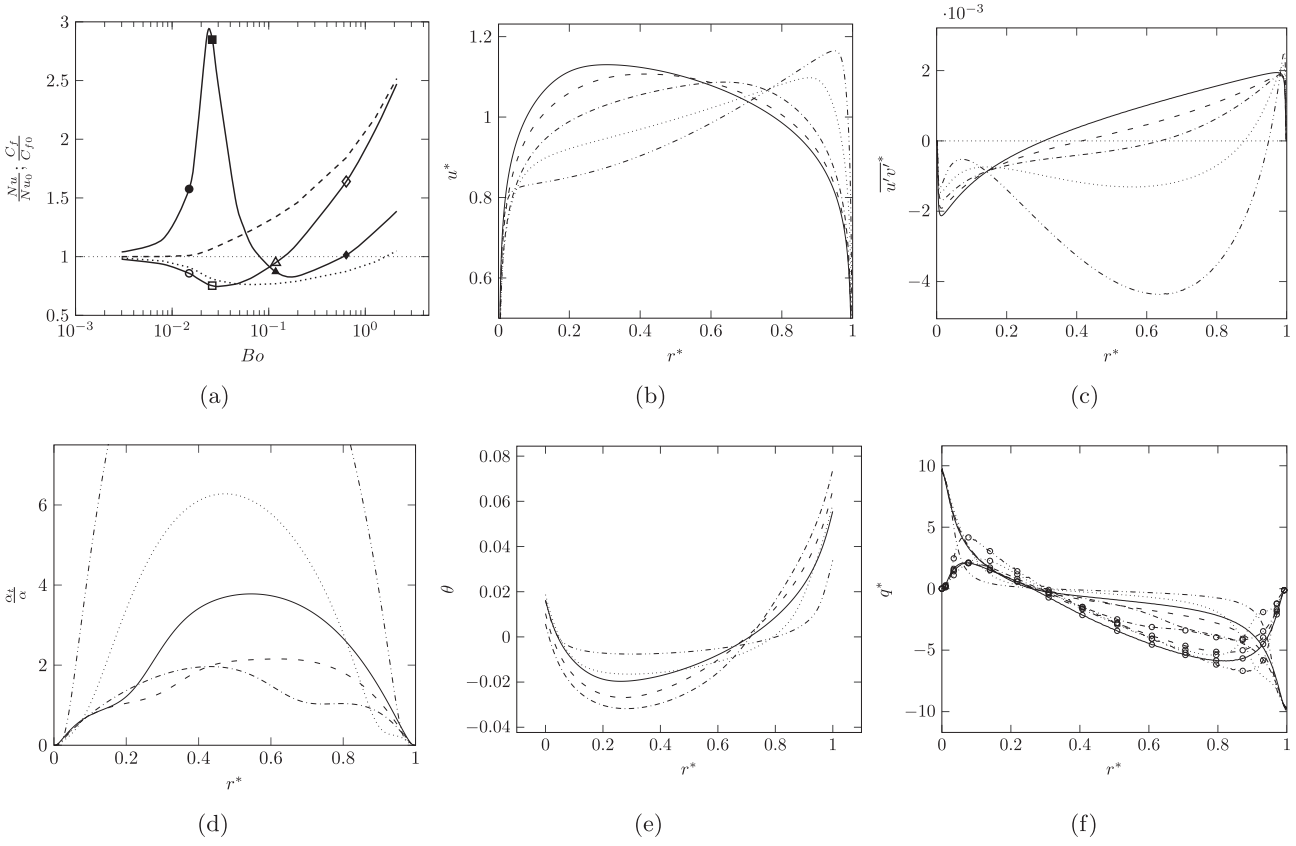

Fig. 9. Both walls heated for $Pr = 0.021$ and $\delta = 0.13$ at (——) $Bo = 0$; (- - - -) $Bo = 0.015$; (-·-·-·) $Bo = 0.026$; (·····) $Bo = 0.118$; (-·· -··) $Bo = 0.635$ (a) Mixed-to-forced Nusselt number ratio: (—— and filled symbols) inner wall; (—— and open symbols symbols) outer wall; Skin friction ratio: (- - - -) outer wall; (·····) inner wall; (b) Mean velocity profiles; (c) Reynolds stresses; (d) Turbulent-to-molecular diffusion; (e) non-dimensional temperature; (f) Molecular heat flux (lines without ○) and turbulent heat flux (lines with ○).

profiles. The temperature gradient close to the inner wall decreases and the non-dimensional inner wall temperature increases to fulfill Eq. (26). From the definition of the non-dimensional temperature, θ, it derives that $\theta_{wi} = 1/Nu_{wi}$. Therefore, the Nusselt number on the inner wall decreases even though the values of α_t/α increase, as shown in Fig. 9a and d for $Bo = 0.118$. By further increasing the Bo number, the turbulent contribution to heat transfer becomes predominant and the Nusselt number increases monotonically on both walls. At $Bo = 0.635$ there is a complete recovery also on the inner surface. The turbulence contribution is now much higher than for forced convection, as shown in Fig. 9c-d and f by the high values of $\overline{u'v'}^*$, α_t/α and $\overline{v'T'}^*$ and in Fig. 9e by the flattened profiles of θ.

As previously done in Section 6.2.1 for the inner heated wall at $\delta = 0.13$, it is also here instructive to make a comparison with a fluid having $Pr = 0.85$, for which turbulent heat transfer is the main energy exchange mechanism. As shown in Fig. 10a the Nusselt number ratio decreases here at both walls and actually more on the inner heated surface. As shown in Fig. 10b and c, at $Bo = 0.3$ the non-dimensional velocity profile is quite flat for $r^* \leqslant 0.2$ resulting in small velocity gradients, small Reynolds stresses and thus small turbulent kinetic energy production and turbulent kinetic energy. This implies vanishingly small values of α_t/α in the immediate wall vicinity, as shown in Fig. 10d. Due to the very thin viscous thermal sublayer on the inner wall, also recognizable from the very steep non-dimensional temperature profiles of Fig. 10e, this region of extremely reduced turbulent mixing extends to r^* where the turbulent heat fluxes are the main heat transfer mechanism. As shown in Fig. 11, even if on the outer wall the impairment of α_t/α extends further into the flow, the magnitude of α_t does not drop to zero as on the inner wall. Here, as shown in Fig. 12, the turbulent heat fluxes for $Bo = 0.3$ are extremely reduced up to $r^* \approx 0.03$, while in the same region they are the main contribution to heat transfer at the other buoyancy numbers. On the outer wall the decrease of $\overline{v'T'}^*$ happens uniformly for all Bo numbers. This explains the minimum value of Nu/Nu_0 observed on the inner wall, as shown in Fig. 10a.

Contrarily to liquid metals, where the high molecular thermal conductivity and heat fluxes can compensate for the reduced turbulent ones, for higher Prandtl number fluids a reduction of $\overline{v'T'}^*$ causes a heat transfer impairment and consequently a decrease of the Nusselt number. The explanation for the values of C_f/C_{f0} on inner and outer wall follow the same reasoning as previously discussed for a liquid metal.

6.2.6. Both walls heated and $\delta = 0.5$

In this case both walls have comparable sizes and heat rates. This results in almost symmetrical profiles of $\overline{u'v'}^*$, u^*, α_t/α, θ and of the magnitude of $\overline{v'T'}^*$, as shown in Fig. 13b–f. Furthermore, at sufficiently high Bo numbers the velocity profiles assume the typical M-shape of turbulent mixed convection in round pipes [2]. The decrease of α_t/α and thus of the turbulent heat fluxes is now markedly higher and extends over the whole cross section for $Bo = 0.018$ and $Bo = 0.070$, this last corresponding approximately to the maximum heat transfer impairment. It should also be noted

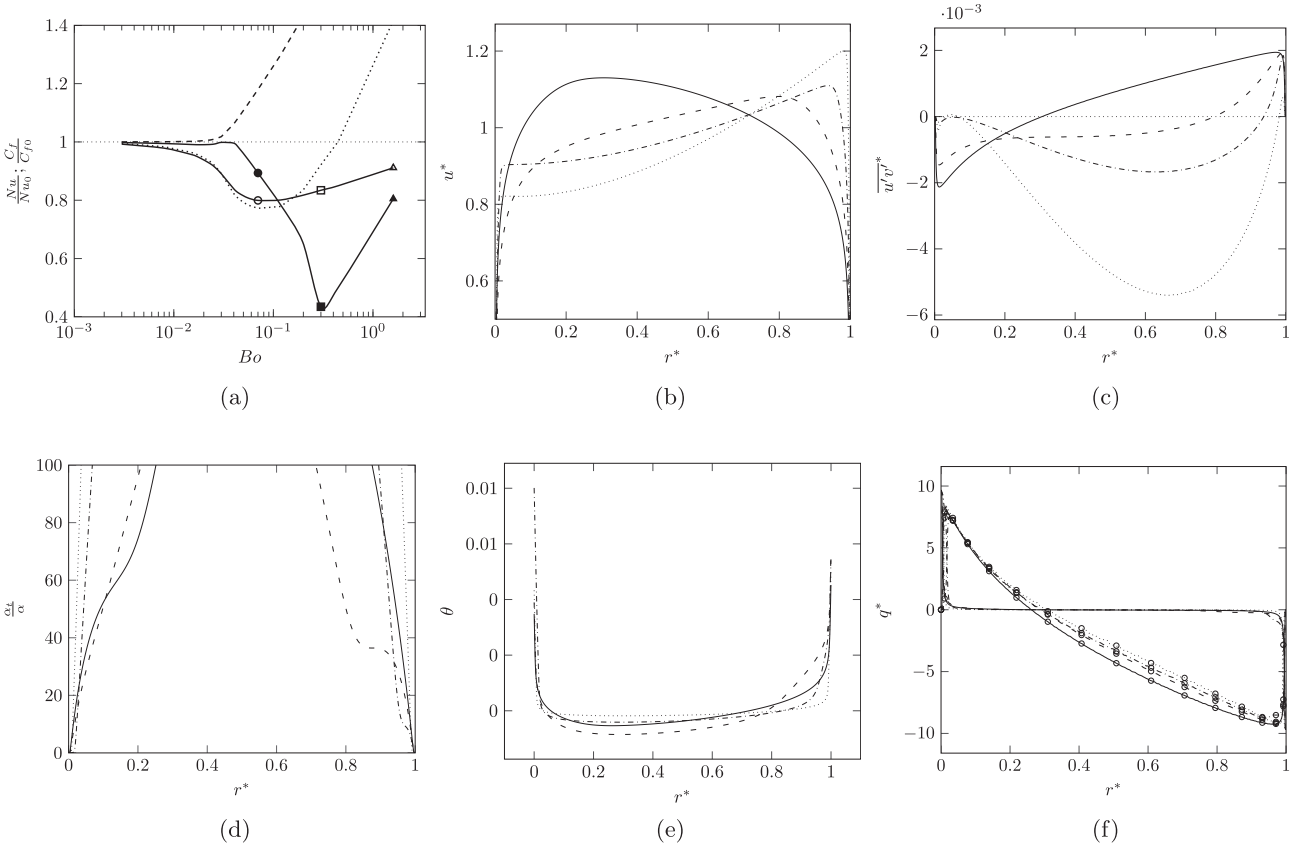

Fig. 10. Both wall heated for $Pr = 0.85$ and $\delta = 0.13$ at (——) $Bo = 0$; (- - - -) $Bo = 0.007$; (-·-·-·-) $Bo = 0.30$; (·····) $Bo = 1.6$ (a) Mixed-to-forced Nusselt number ratio: (—— and filled symbols) inner wall; (—— and open symbols symbols) outer wall; Skin friction ratio: (- - - -) outer wall; (·····) inner wall; (b) Mean velocity profiles; (c) Reynolds stresses; (d) Turbulent-to-molecular diffusion; (e) non-dimensional temperature; (f) Molecular heat flux (lines without ○) and turbulent heat flux (lines with ○).

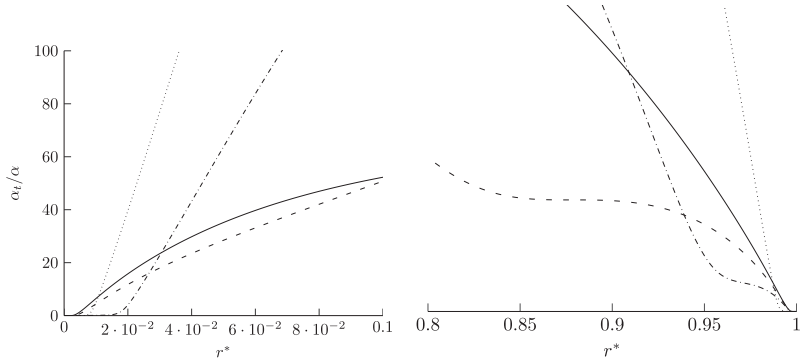

Fig. 11. Zoom of α_t/α close to the inner (left) and outer (right) wall for $Pr = 0.85$ and $\delta = 0.13$; Lines defined in Fig. 10d.

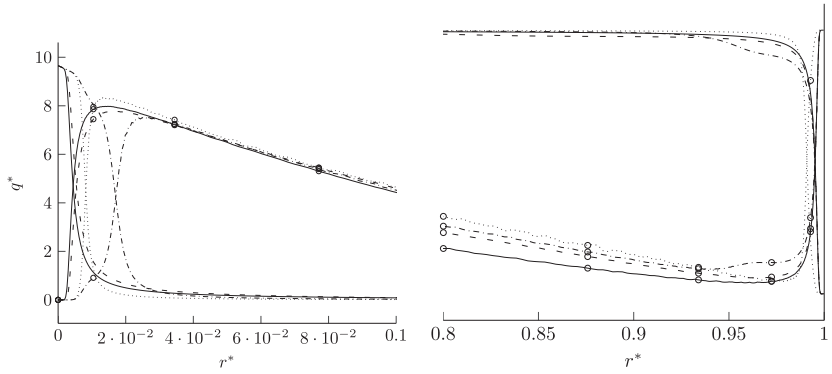

Fig. 12. Zoom of molecular and turbulent heat fluxes close to the inner (left) and outer (wall) for $Pr = 0.85$ and $\delta = 0.13$; Lines defined in Fig. 10f.

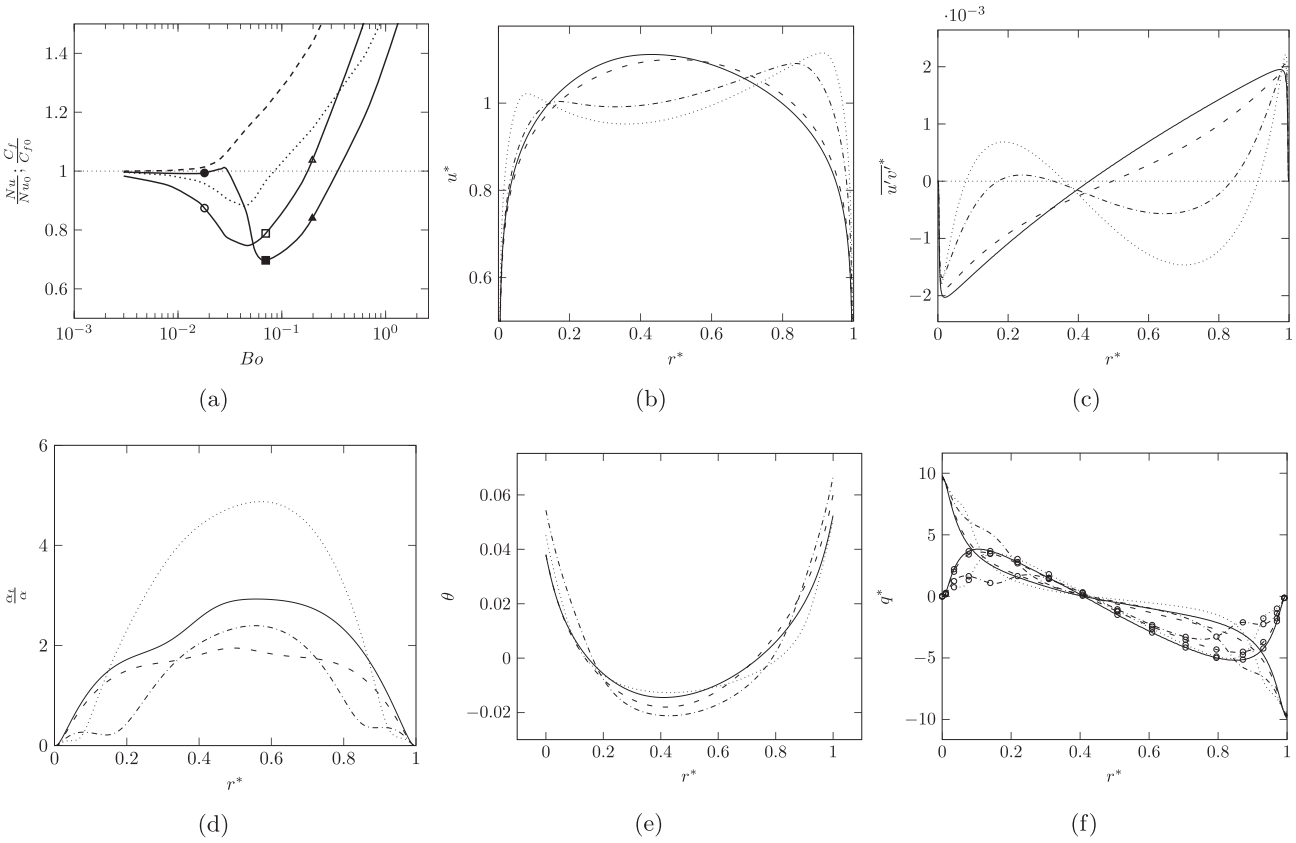

Fig. 13. Both walls heated for $Pr = 0.021$ and $\delta = 0.5$ at (——) $Bo = 0$; (- - - -) $Bo = 0.018$; (-·-·-) $Bo = 0.070$; (·····) $Bo = 0.197$ (a) Mixed-to-forced Nusselt number ratio: (—— and filled symbols) inner wall; (—— and open symbols symbols) outer wall; Skin friction ratio: (- - - -) outer wall; (·····) inner wall; (b) Mean velocity profiles; (c) Reynolds stresses; (d) Turbulent-to-molecular diffusion; (e) non-dimensional temperature; (f) Molecular heat flux (lines without ○) and turbulent heat flux (lines with ○).

that the curves of Nu/Nu_0 for inner and outer wall do not overlap but are practically shifted horizontally, being the onset of heat transfer impairment on the inner wall delayed. Indeed, the values of α_t/α for $Bo = 0$ are lower on the inner region than on the outer one, as shown in Fig. 13d. Compared to forced convection, at $Bo = 0.018$ the decrease of the values of α_t/α on the inner region is then smaller than the corresponding one close to the outer wall. Consequently, the heat transfer impairment occurs later on the inner wall, i.e. for higher Bo numbers. At the same Bo number the magnitude of the turbulent heat fluxes on the inner wall is smaller than that on the outer one, as shown in Fig. 13f. This results in lower values of Nu/Nu_0 on the inner wall. The temperature profiles shown in Fig. 13e are quite rounded for $Bo = 0, Bo = 0.018$ and $Bo = 0.070$. With increasing Bo, the turbulent mixing in the core region increases, as shown by the higher values of α_t/α. Thus, the temperature profiles become flatter, as shown by the curve for $Bo = 0.197$ of Fig. 13e.

As shown in Fig. 13a, C_f/C_{f0} on the outer wall increases monotonically with increasing Bo. Indeed, the higher velocity gradients always prevail over the reduced turbulent momentum diffusivity. Contrarily, on the inner wall the reduced turbulent mixing causes C_f/C_{f0} first to decrease and then to recover with increasing Bo. Anyway, this reduction is much less pronounced than that of Nu/Nu_0.

7. Conclusions

Within this work a detailed numerical analysis of the turbulent aided mixed convection of a liquid metal with $Pr = 0.021$ flowing in a concentric annulus has been performed. The buoyancy effects have been accounted for in the momentum equation using the Boussinesq approximation. Four different eddy-viscosity low-Reynolds turbulence models have been considered. The turbulent heat fluxes have been modeled with the Simple-Gradient-Diffusion-Hypothesis. To compute the turbulent Prandtl number either a correlation has been adopted or two additional transport equations have been solved. The performance of the models has first been assessed against experimental data of a pipe flow. Best results are obtained by employing the correlation of Kays [27] to locally evaluate Pr_t. Even though it has been derived and tested for forced convection it also performs well for ascending turbulent mixed convection in a pipe. More validation data are needed to draw a final conclusion on its applicability to mixed convection flows. Nevertheless, according to the present results it can be recommended. The model of Launder and Sharma [19] with the correlation of Kays [27] has then been selected for all subsequent computations.

Simulations of the fully developed pipe flow have highlighted for liquid metals a noteworthy dependency from the Péclet number of the onset and degree of heat transfer impairment. Beyond $Pe = 2500$ no significant difference is observed. Accordingly, $Pe = 3000$ has been chosen for the analysis of the concentric annulus in order to obtain more general results.

According to the studies of turbulent ascending mixed convection in a pipe with air or water [1,6,10,12–14], the onset of heat transfer impairment occurs at approximately $Bo = 0.1$ and the complete recovery, i.e. $Nu/Nu_0 = 1$, at $Bo = 3$. From the present results for a pipe geometry it can be immediately recognized that the region of heat transfer impairment is now restricted to a much lower range of Bo numbers, namely $0.02 \leqslant Bo \leqslant 0.2$. Moreover, the magnitude of the maximum heat transfer impairment is less than for medium-to–high Prandtl number fluids.

Table 6
Summary of results of concentric annulus simulations of Section 6.2; q_{wi} inner wall heated; q_{wo} outer wall heated; $q_{wi,wo}$ both walls heated; (wi) values refer to inner wall; (wo) values refer to outer wall.

			Onset			Laminarization			Recovery		
	δ		Bo	Nu/Nu_0	C_f/C_{f0}	Bo	Nu/Nu_0	C_f/C_{f0}	Bo	Nu/Nu_0	C_f/C_{f0}
q_{wi}	0.13		–	–	–	–	–	–	–	–	–
	0.13	$Pr = 0.85$	0.003	0.987	1.042	0.018	0.970	1.232	0.317	1.038	2.386
	0.50		0.002	0.980	1.045	0.006	0.970	1.125	0.011	1.000	1.204
q_{wo}	0.13		0.002	0.980	1.000	0.018	0.794	1.057	0.118	1.080	1.384
	0.50		0.002	0.973	1.008	0.015	0.887	1.107	0.040	1.000	1.250
$q_{wi,wo}$	0.13 (wi)		0.118	0.900	0.768	0.197	0.833	0.789	0.635	1.014	0.873
	0.13 (wo)	$Pr = 0.85$	0.045	0.980	0.803	0.300	0.435	0.920	1.600	0.800	1.415
	0.13 (wo)		0.003	0.980	1.000	0.030	0.746	1.090	0.197	1.100	1.458
	0.13 (wo)	$Pr = 0.85$	0.008	0.980	1.000	0.070	0.800	1.800	1.600	0.910	2.350
	0.50 (wi)		0.045	0.866	0.877	0.070	0.696	0.965	0.635	1.190	1.392
	0.50 (wo)		0.003	0.980	1.000	0.045	0.747	1.143	0.197	1.036	1.437

The results of the analysis on the concentric annulus are summarized in Table 6. Three different situations are considered, namely the onset of heat transfer impairment, the maximum heat transfer impairment or laminarization and the recovery, this last identified by the Bo number at which $Nu/Nu_0 \approx 1$.

When only the inner wall is heated, the mixed-to-forced friction factor ratio on it shows a monotonic increase for $Pr = 0.021$ as well as for $Pr = 0.85$ independently from the radius ratio. The same increasing trend of C_f/C_{f0} is also found for $Pr = 0.021$ when only the outer wall is heated. When both walls are heated the friction factor on the inner wall first decreases and then recovers at higher Bo numbers. The reason lies in the initial strong reduction of turbulent momentum diffusivity together with the reduced velocity gradients. Contrarily, on the outer wall the higher velocity gradients always overcome the reduced turbulent mixing and thus C_f/C_{f0} monotonically increases. When present, the reduction of C_f/C_{f0} is typically significantly lower than that of Nu/Nu_0. From this picture the dissimilarity between momentum transfer and heat transfer is evident.

Generally, it can be concluded that for liquid metals, due to the low values of α_t/α, the onset of heat transfer impairment occurs at lower Bo numbers than for medium-to–high Prandtl number fluids. Indeed, even a small decrease in turbulence intensity affects the heat transfer, while for higher Prandtl numbers this has to be more pronounced because of the very high turbulent-to-molecular thermal diffusivity ratio. Moreover, the higher contribution of the molecular heat flux dampen the reduction of the turbulent one resulting in a smaller heat transfer impairment compared to medium-to–high Prandtl number fluids. For liquid metals the recovery occurs earlier because the modified velocity profile and the consequently enhanced molecular contribution to heat transfer close to the wall can overcome the reduced turbulent heat fluxes. Contrarily, for medium-to–high Prandtl number fluids, due to the predominance of turbulent heat transfer, the recovery only occurs when the values of α_t/α, and thus of the turbulent heat fluxes, become practically everywhere higher than those at the maximum impairment.

From the experimental data of Nu/Nu_0 determined by Buhr et al. [4] for aided mixed convection of mercury in a pipe it could be concluded that the family of fluids with $Pr \approx 0.025$ behave, at least qualitatively, like medium-to–high Prandtl number fluids under mixed convection effects [3]. The same conclusion is not supported by the present results for a concentric annulus. Indeed, for a radius ratio of $\delta = 0.13$ and when only the inner wall is heated there is no heat transfer impairment for fluids with $Pr = 0.021$ and Nu/Nu_0 increases monotonically. The same is not true when $Pr = 0.85$, where a small heat transfer impairment is found, as also shown in Table 6. For both walls heated and $\delta = 0.13$ there is heat transfer impairment and successive recovery on the inner and outer wall for $Pr = 0.85$. For $Pr = 0.021$ at the same Bo of maximum heat transfer impairment on the outer wall, there is instead a peak of Nu/Nu_0 on the inner wall with a successive decrease when the heat transfer recovers on the other wall. Moreover, also the values of Nu/Nu_0 at laminarization are typically lower for liquid metals and the recovery is achieved much earlier, i.e. at smaller Bo numbers. The explanation for this discrepancy resides in the different contribution to heat transfer for liquid metals. Indeed, due to their extremely high molecular thermal conductivity compared to ordinary fluids, the molecular contribution to heat transfer extends over a considerable portion of the cross section and can therefore partly compensate the decrease of turbulent heat fluxes.

In order to better assess turbulence models for the turbulent mixed convection to liquid metals either exhaustive experimental data or "numerical data" from Direct Numerical Simulations would be beneficial. To the authors' knowledge the only experimental data available in literature are still those of Buhr et al. [4] of 1974, which are also not much extensive. The reason also lies in the difficulties related to the experimental setup for these fluids. On the other side, other than for fluids with $Pr \sim \mathcal{O}(1)$ [2], there is no DNS available for mixed convection to liquid metals. The problem is that for low-Pr number fluids high Reynolds numbers are needed for the turbulent heat fluxes to play a major role. Consequently very high computational resources are necessary.

Several aspects emerging from the present analysis, that can be also useful recommendations for simulating and designing buoyant liquid metal flow systems, are here summarized:

- As already found for medium-to–high Prandtl number fluids, also for liquid metal flows two-equations eddy viscosity models can reproduce fairly well the modifications of the velocity and turbulence fields under mixed convection effects
- At least for attached wall bounded liquid metal flows the heat fluxes can be modeled according to the concept of the turbulent Prandtl number, with the correlation proposed by Kays [27] for forced convection. For other more complex configurations, e.g. with separation/reattachment and anisotropy in the Reynolds stresses and turbulent heat fluxes, a further validation is necessary
- A more sophisticated k-ε-k_θ-ε_θ model for evaluating Pr_t in liquid metal flows, developed and tested for forced convection, did not perform as well as the simpler approach with a proper correlation. This fact shows for liquid metals the difficulties and risks of extrapolating simulation approaches valid for forced convection to mixed convection
- Compared to medium-to–high Prandtl number fluids, liquid metals are much more sensitive to the Péclet (or Reynolds) number of the flow for the onset, laminarization and recovery

of heat transfer. This should be strictly considered when extrapolating results from high to low *Pe* (or *Re*) numbers
- The heat transfer impairment in liquid metals occurs for a narrower range of *Bo* numbers compared to medium-to–high Prandtl number fluids. Moreover the magnitude of this impairment is also smaller
- Due to the heat transfer mechanism of liquid metals, resulting in an enhanced contribution of the conductive heat transfer over the turbulent one, even for the same geometry and boundary conditions the results and conclusions obtained for medium-to–high Prandtl number fluids cannot be extrapolated to the case of liquid metal flows

Acknowledgements

The authors wish to acknowledge the support of the Helmholtz Association in the framework of the Helmholtz-Alliance LIMTECH (Liquid Metal Technology), Subtopic B2: Liquid Metals for Solar Power Systems.

The authors acknowledge the help of Mr. Damir Rigler for the programming of the turbulence models in OpenFOAM.

References

[1] J. Jackson, M. Cotton, B.P. Axcell, Studies of mixed convection in vertical tubes, Int. J. Heat Fluid Flow 10 (1989) 2–15.
[2] J. You, J.Y. Yoo, H. Choi, Direct numerical simulation of heated vertical air flows in fully developed turbulent mixed convection, Int. J. Heat Mass Transfer 46 (2003) 1613–1627.
[3] J. Jackson, B. Axcell, A. Walton, Mixed convection heat transfer to sodium in a vertical pipe, Exp. Heat Transfer 7 (1994) 71–90.
[4] H.O. Buhr, E.A. Horsten, A.D. Carr, The distortion of turbulent velocity and temperature profiles on heating, for mercury in a vertical pipe, ASME J. Heat Transfer 96 (1974) 152–158.
[5] M. Cotton, J. Jackson, L. Yu, Application of a low-Reynolds-number two-equation turbulence model to mercury and sodium flows in the turbulent mixed convection regime, in: 7th Symposium on turbulent shear flows, 1989.
[6] W. Kim, C. Talbot, B. Chung, J. Jackson, Variable property mixed convection heat transfer to air flowing through a vertical passage of annular cross section: part 1, Chem. Eng. Res. Des. 80 (2002) 239–245.
[7] J. Wang, J. Li, J. Jackson, Mixed convection heat transfer to air flowing upwards through a vertical plane passage: part 3, Chem. Eng. Res. Des. 80 (2002) 252–260.
[8] T.-H. Wu, Z. Xu, J. Jackson, Mixed convection heat transfer to water flowing through a vertical passage of annular cross section: part 2, Chem. Eng. Res. Des. 80 (2002) 246–251.
[9] Y. Parlatan, N.E. Todreas, M.J. Driscoll, Buoyancy and property variation effects in turbulent mixed convection of water in vertical tubes, ASME J. Heat Transfer 118 (1996) 381–387.
[10] G.P. Celata, F. Dannibale, A. Chiaradia, M. Cumo, Upflow turbulent mixed convection heat transfer in vertical pipes, Int. J. Heat Mass Transfer 41 (1998) 4037–4054.
[11] J. Jackson, Turbulent mixed convection heat transfer to liquid sodium, Int. J. Heat Fluid Flow 4 (1983) 107–111.
[12] T. Aicher, H. Martin, New correlations for mixed turbulent natural and forced convection heat transfer in vertical tubes, Int. J. Heat Mass Transfer 40 (1997) 3617–3626.
[13] M. Cotton, J. Jackson, Vertical tube air flows in the turbulent mixed convection regime calculated using a low-Reynolds-number $k-\varepsilon$ model, Int. J. Heat Mass Transfer 33 (1990) 275–286.
[14] A. Keshmiri, Effects of various physical and numerical parameters on heat transfer in vertical passages at relatively low heat loading, ASME J. Heat Transfer 133 (2011) 1–8.
[15] P. Forooghi, I.A. Abdi, M. Dahari, K. Hooman, Buoyancy induced heat transfer deterioration in vertical concentric and eccentric annuli, Int. J. Heat Mass Transfer 81 (2015) 222–233.
[16] J.H. Bae, J.Y. Yoo, H. Choi, Direct numerical simulation of turbulent supercritical flows with heat transfer, Phys. Fluids 17 (2005).
[17] K. Rehme, Convective heat transfer over rod bundles, in: S. Kakaç, R.K. Shah, W. Aung (Eds.), Handbook of Single-Phase Convective Heat Transfer, John Wiley & Sons, 1987.
[18] W. Kim, S. He, J. Jackson, Assessment by comparison with DNS data of turbulence models used in simulations of mixed convection, Int. J. Heat Mass Transfer 51 (2008) 1293–1312.
[19] B. Launder, B. Sharma, Application of the energy-dissipation model of turbulence to the calculation of flow near a spinning disc, Lett. Heat Mass Transfer 1 (1974) 131–137.
[20] K. Abe, T. Kondoh, Y. Nagano, A new turbulence model for predicting fluid flow and heat transfer in separating and reattaching flows–I. Flow field calculations, Int. J. Heat Mass Transfer 37 (1994) 139–151.
[21] P. Durbin, Separated flow computations with the $k-\epsilon$ and $v^2\overline{}$ model, AIAA J. 33 (1995) 659–664.
[22] F.-S. Lien, G. Kalitzin, Computations of transonic flow with the v^2-f turbulence model, Int. J. Heat Fluid Flow 22 (2001) 53–61.
[23] L. Davidson, P. Nielsen, A. Sveningsson, Modifications of the V2F model for computing the flow in a 3D wall jet, in: K. Hanjalic, Y. Nagano, M. Tummers (Eds.), Turbulence Heat and Mass Transfer, Begell House Inc., 2003.
[24] K. Rehme, Turbulent flow in smooth concentric annuli with small radius ratios, J. Fluid Mech. 64 (1974) 263–288.
[25] G. Grötzbach, Challenges in low-Prandtl number heat transfer simulation and modelling, Nucl. Eng. Des. (2013) 41–55.
[26] L. Marocco, G. Cammi, J. Flesch, T. Wetzel, Numerical analysis of a solar tower receiver tube operated with liquid metals, Int. J. Therm. Sci. 105 (2016) 22–35.
[27] W. Kays, Turbulent Prandtl number – Where are we?, ASME J Heat Transfer 116 (1994) 284–295.
[28] M. Duponcheel, L. Bricteux, M. Manconi, G. Winckelmans, Y. Bartosiewicz, Assessment of RANS and improved near-wall modeling for forced convection at low prandtl numbers based on LES up to $Re_\tau = 2000$, Int. J. Heat Mass Transfer 75 (2014) 470–482.
[29] S. Manservisi, F. Menghini, A CFD four parameter heat transfer turbulence model for engineering applications in heavy liquid metals, Int. J. Heat Mass Transfer 69 (2014) 312–326.
[30] S. Manservisi, F. Menghini, Triangular rod bundle simulations of a CFD k-ε-$k_\theta - \varepsilon_\theta$ heat transfer turbulence model for heavy liquid metals, Nucl. Eng. Des. 273 (2014) 251–270.
[31] A. Alberti di Valmontana, Numerical simulation with RANS models of the ascending turbulent mixed convection to liquid metals flowing in a concentric annulus, Master's thesis, Politecnico di Milano, 2016.
[32] L. Marocco, A. Loges, T. Wetzel, R. Stieglitz, Experimental investigation of the turbulent heavy liquid metal heat transfer in the thermal entry region of a vertical annulus with constant heat flux on the inner surface, Int. J. Heat Mass Transfer 55 (2012) 6435–6445.
[33] J. Pacio, L. Marocco, T. Wetzel, Review of data and correlations for turbulent forced convective heat transfer of liquid metals in pipes, Heat Mass Transfer 51 (2015) 153–164.
[34] X. Cheng, N.-i. Tak, Investigation on turbulent heat transfer to lead–bismuth eutectic flows in circular tubes for nuclear applications, Nucl. Eng. Des. 236 (2006) 385–393.
[35] T. Schulenberg, R. Stieglitz, Flow measurement techniques in heavy liquid metals, Nucl. Eng. Des. 240 (2010) 2077–2087.
[36] F. Roelofs, A. Shams, I. Otic, M. Böttcher, M. Duponcheel, Y. Bartosiewicz, D. Lakehal, E. Baglietto, S. Lardeau, X. Cheng, Status and perspective of turbulence heat transfer modelling for the industrial application of liquid metal flows, Nucl. Eng. Des. 290 (2015) 99–106.
[37] S. Patankar, C. Liu, E. Sparrow, The periodic thermally developed regime in ducts with streamwise periodic wall temperature or heat flux, Int. J. Heat Mass Transfer 21 (1978) 557–566.
[38] J. Ferziger, M. Perić, Computational Methods for Fluid Dynamics, 3 ed., Springer, Berlin Heidelberg, 2001.
[39] I. Celik, U. Ghia, P. Roache, C. Freitas, H. Coleman, P. Raad, Procedure for estimation and reporting of uncertainty due to discretization in CFD applications, ASME J. Fluids Eng. 130 (7) (2008).
[40] H. Buhr, A. Carr, R. Balzhiser, Temperature profiles in liquid metals and the effect of superimposed free convection in turbulent flow, Int. J. Heat Mass Transfer 11 (1968) 641–654.
[41] L. Hochreiter, A. Sesonske, Turbulent structure of isothermal and non-isothermal liquid metal pipe flow, Int. J. Heat Mass Transfer 17 (1974) 113–123.